IMAGING SMALL POLARIZABLE SCATTERERS WITH POLARIZATION DATA

PATRICK BARDSLEY

MAXENCE CASSIER

Aix Marseille Univ, CNRS, Centrale Marseille, Institut Fresnel, Marseille, France; Department of Applied Physics and Applied Mathematics, Columbia University, New York, NY 10027, United States.

FERNANDO GUEVARA VASQUEZ

Mathematics Department, University of Utah, 155 S 1400 E RM 233, Salt Lake City UT 84112-0090.

ABSTRACT. We present a method for imaging small scatterers in a homogeneous medium from polarization measurements of the electric field at an array. The electric field comes from illuminating the scatterers with a point source with known location and polarization. We view this problem as a generalized phase retrieval problem with data being the coherency matrix or Stokes parameters of the electric field at the array. We introduce a simple preprocessing of the coherency matrix data that partially recovers the ideal data where all the components of the electric field are known for different source dipole moments. We prove that the images obtained using an electromagnetic version of Kirchhoff migration applied to the partial data are, for high frequencies, asymptotically identical to the images obtained from ideal data. We analyze the image resolution and show that polarizability tensor components in an appropriate basis can be recovered from the Kirchhoff images, which are tensor fields. A time domain interpretation of this imaging problem is provided and numerical experiments are used to illustrate the theory.

1. INTRODUCTION

We consider the problem of imaging a collection of small dielectric scatterers by illuminating the scene with a point source whose location is known but that is driven by a random process with known statistical properties. This is a common

assumption in optics, where it is easier to measure polarization, which is a statistical property of light. The data we use for imaging is also the polarization measured at an array of receivers. The polarization state of a wave measured on the plane x_1, x_2 can be described by the coherency matrix (see e.g. [39]), which is the 2×2 Hermitian matrix of correlations between the x_1, x_2 components of the frequency domain electric field $\boldsymbol{E}(\boldsymbol{x}_r, \omega)$:

$$(1) \qquad \boldsymbol{\Psi} = \langle \boldsymbol{E}_\| \boldsymbol{E}_\|^* \rangle,$$

where $\langle \cdot \rangle$ denotes the average over many realizations and $\boldsymbol{E}_\| \equiv [E_1, E_2]^T$. An equivalent description of the polarization is the so called *Stokes parameters*:

$$(2)$$
$$I = \langle |E_1|^2 + |E_2|^2 \rangle, \ Q = \langle |E_1|^2 - |E_2|^2 \rangle, \ U = \langle 2\mathrm{Re}(E_1 \overline{E_2}) \rangle, \ \text{and } V = \langle 2\mathrm{Im}(E_1 \overline{E_2}) \rangle.$$

Thus the polarization data we assume corresponds to a *four dimensional real field* defined over the array. This field can be measured directly by a conventional CMOS sensor with successive experiments involving a combination of linear polarizers and quarter-wave plates, see e.g. [10].

We think of the problem at hand as a vector analogue to imaging with intensities only. Indeed, suppose that we had full control of the phase and amplitude of the dipole moment describing the source and that we could measure both amplitudes and phases of the x_1, x_2 components of the electric field at the array. Then we could perform experiments with linearly independent dipole moments and the data at the array would be a 2×2 complex matrix field, or equivalently an *8 dimensional real field*. Thus by using polarization data *we are foregoing half of the degrees of freedom* compared to this ideal case. This is similar to intensity only imaging, where only a one dimensional quantity (the magnitude or intensity) is measured for a two dimensional quantity (the complex representation of a scalar field). The other similarity with intensity measurements is that the coherency matrix (1) is a quadratic form of the data.

The strategy we use for imaging generalizes the approach for scalar waves in [9] and consists of preprocessing the polarization data to approximate the ideal data. Since the preprocessing creates an 8 dimensional real field from a 4 dimensional one, there are very significant errors. The key is to show that these errors do not affect images of the scatterers, if we use an electromagnetic version of Kirchhoff imaging [18]. We do this with a stationary phase argument. The images we obtain are 2×2 complex matrix fields that contain information about the polarizability tensors of the scatterers, projected onto an appropriate basis that is dictated by the relative positions of the source, the array and the scatterers.

1.1. **Related work.** The resolution analysis of the electromagnetic version of Kirchhoff migration we present here adapts the analysis in [18] to the case of an array receivers with a source away from the array. The conclusion of [18] is that well known spatial resolution estimates that hold for acoustics (see e.g. [11]) also hold in electromagnetics. The recovery of polarizability tensor information from Kirchhoff migration images was done in [18], where the data was collected for a collocated array of sources and receivers. In our case the sources and the receivers are at different locations and thus the components of the polarizability tensor that can be stably recovered differ.

There are other methods for imaging small scatterers in electromagnetics, including methods using MUSIC [24] such as [3, 1, 12]. The effect of noise on the

MUSIC images has been analyzed using random matrix theory in [12]. Imaging small scatterers is related to the selective focusing problem considered in [6].

The problem of finding the electric field from coherency matrix data is a generalization of the phase retrieval problem. This is a classic problem in optics where phases are typically much harder to measure than intensities. Here we give a non-exhaustive overview of methods for solving the phase retrieval problem or imaging without phases. We focus on approaches that are the closest to the method we present here. In specific situations, uniqueness is guaranteed [36, 37, 35]. Methods for solving this problem include iterative methods that approximatively recover phases [32], redundant expansion in frames [17, 7] and sparsity promoting algorithms that exploit the sparsity of an image made of point scatterers, see e.g. [20, 16, 47].

A key aspect of our imaging method is that we do not need to retrieve all phases from the data, since the imaging method we use does not require it. This is a feature that is also used for intensity only imaging in [42, 40, 41, 9, 8]. For full aperture data, phase retrieval is done in [22, 23, 21] using a similar preprocessing of the intensity data as we present here. One novelty in our method is that we image polarizability of scatterers, directly from polarization data. There are other ways of imaging polarizability in different physical setups such as Optical Coherence Tomography from interferometric data [26] and Polarimetric Synthetic Aperture Radar (see e.g. [27]). Finally we point out that our imaging method can be seen as correlation based imaging, see e.g. [44, 28, 29, 31].

Throughout this paper we assume the scatterers are point-like. This is a reasonably good approximation as can be seen from small diameter asymptotic analysis [45, 5, 4]. The expansion can actually be carried further in terms of powers of the diameter and can be used for reconstruction, see e.g. [2].

1.2. **Contents.** We start by describing two imaging problems in section 2: (a) the ideal "full data" case where we can control both the amplitudes and phases of the source and the receivers and (b) the case where they are random and we only know their statistical properties. In section 3 we introduce the electromagnetic version of Kirchhoff imaging (that assumes full data is available) and define the preprocessing step that takes polarization data and gives an approximation of the full data that can be used for imaging. We prove in section 4 that in the high frequency limit, the Kirchhoff image of the preprocessed polarization data is asymptotically identical to the image obtained with full data. In section 5 we do a resolution analysis of Kirchhoff imaging for electromagnetic waves, that generalizes the results obtained in [18] to the case where the sources and receivers are not collocated. All the analysis up to this point is done in the frequency domain. The connection with the time domain is done in section 6, where we show that polarization data can also be obtained by measuring autocorrelations of the time domain electric field over long periods of time. Our theoretical results are illustrated with numerical experiments in section 7. We conclude with a discussion and perspectives for future work in section 8.

2. Problem setup

The experiment we consider is depicted in fig. 1. We illuminate a family of point-like scatterers located at $\boldsymbol{y}_1, \ldots, \boldsymbol{y}_n \in \mathbb{R}^3$, with the field emanating from an electric dipole at a known location $\boldsymbol{x}_s$. We measure the electric field at an array
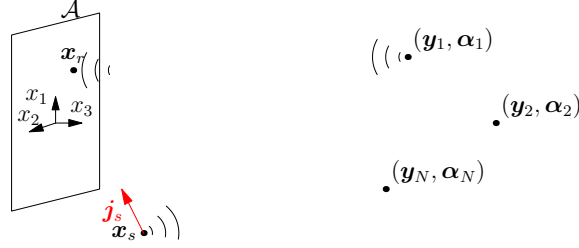
FIGURE 1. We seek to image the position and polarizability tensors of a collection of point scatterers at locations $\boldsymbol{y}_1, \ldots, \boldsymbol{y}_n$ from measurements of the electric field made at an array $\mathcal{A}$. The medium is illuminated by an electric dipole at a known position $\boldsymbol{x}_s$ with polarization $\boldsymbol{j}_s$.

$\mathcal{A}$ located in the $x_3 = 0$ plane. In the following, we denote by ε the dielectric permittivity, μ the magnetic permeability, $c = (\varepsilon\mu)^{-1/2}$ the wave propagation of the medium (assumed to be homogeneous), ω the angular frequency and $k = \omega/c$ the wavenumber. We use the convention

$$(3) \quad \boldsymbol{E}(\boldsymbol{x}; t) = \int d\omega \, \boldsymbol{E}(\boldsymbol{x}; \omega) \exp[-\imath\omega t] \text{ and } \boldsymbol{E}(\boldsymbol{x}; \omega) = \frac{1}{2\pi} \int dt \, \boldsymbol{E}(\boldsymbol{x}; t) \exp[\imath\omega t],$$

to relate the electric field in the time and frequency domain. We assume the symmetry $\boldsymbol{E}(\boldsymbol{x}; -\omega) = \overline{\boldsymbol{E}(\boldsymbol{x}; \omega)}$ so that the time domain electric field is real.

The incident electric field $\boldsymbol{E}_I(\boldsymbol{x}, \omega)$ generated by an electric dipole located at the source point $\boldsymbol{x}_s$ with (possibly complex) *dipole moment* or *polarization vector* $\boldsymbol{j}_s'(\omega) \in \mathbb{C}^3$ is

$$(4) \quad \boldsymbol{E}_I(\boldsymbol{x}; \omega) = \boldsymbol{G}(\boldsymbol{x}, \boldsymbol{x}_s; \omega/c) \boldsymbol{j}_s(\omega),$$

where we use for convenience $\boldsymbol{j}_s(\omega) \equiv \mu\omega^2 \boldsymbol{j}_s'(\omega)$. Hereinafter, when we refer to polarization vector of an electric dipole, we refer to the rescaled $\boldsymbol{j}_s(\omega)$ instead of the physical $\boldsymbol{j}_s'(\omega)$. Here $\boldsymbol{G}(\boldsymbol{x}, \boldsymbol{y}; k)$ is the dyadic Green function of the homogeneous background medium, a 3×3 complex symmetric matrix given by (see e.g. [43])

$$(5) \quad \boldsymbol{G}(\boldsymbol{x}, \boldsymbol{y}; k) = G(\boldsymbol{x}, \boldsymbol{y}; k) \left[(1 + m(kr))\boldsymbol{I} - (1 + 3m(kr))\frac{\boldsymbol{r}\boldsymbol{r}^\top}{r^2} \right]$$

where $G(\boldsymbol{x}, \boldsymbol{y}; k) = \exp[\imath kr]/(4\pi r)$ is the Green function for the scalar Helmholtz equation in 3D, $\boldsymbol{r} = \boldsymbol{x} - \boldsymbol{y}$, $r = |\boldsymbol{x} - \boldsymbol{y}|$ and $m(kr) = (\imath kr - 1)/(kr)^2$.

In this setting, the expression of the total field (incident field plus scattered field) at a receiver is given (see [43]) by

$$(6) \quad \boldsymbol{E}(\boldsymbol{x}_r; \omega) = \boldsymbol{E}_I(\boldsymbol{x}_r; \omega) + \sum_{n=1}^{N} \boldsymbol{G}(\boldsymbol{x}_r, \boldsymbol{y}_n; \omega/c) \, \boldsymbol{\alpha}(\boldsymbol{y}_n; \omega) \, \boldsymbol{E}(\boldsymbol{y}_n; \omega), \forall \boldsymbol{x}_r \in \mathcal{A},$$

where $\boldsymbol{\alpha}(\boldsymbol{y}_n; \omega) \equiv \mu\omega^2 \boldsymbol{\alpha}'(\boldsymbol{y}_n; \omega)$ is the *polarizability* or *polarization tensor* of the scatterer located at $\boldsymbol{y}_n$. The 3×3 complex symmetric matrix $\boldsymbol{\alpha}(\boldsymbol{y}_n; \omega)$ fully characterizes the scattering properties of the $n-$th scatterer. Its analogue in acoustics is the reflection coefficient. We choose to work with the rescaled tensor $\boldsymbol{\alpha}$ since it better reflects the high frequency behavior of the physical polarizability $\boldsymbol{\alpha}'$. Indeed for small penetrable inclusions made of a Drude-Lorentz material, the rescaled $\boldsymbol{\alpha}$

can be regarded as independent of frequency for high frequencies [43]. More generally, this high frequency behavior holds also for a large class of inclusions whose permittivity is characterized by a generalized Lorentz model (i.e., a sum of Lorentz oscillators). Hereinafter, when we refer to the polarizability tensor, we refer to the rescaled $\boldsymbol{\alpha}$, and we assume (for simplicity) that it is constant with respect to ω.

We assume scattering in the medium is sufficiently weak such that the first Born approximation holds (see e.g. [15, 43]). This amounts to taking $\boldsymbol{E}(\boldsymbol{y}_n; \omega) = \boldsymbol{E}_I(\boldsymbol{y}_n; \omega)$ in the right-hand side of eq. (6), along with the assumption that the leading order correction to the first Born approximation (corresponding to second order scattering events) satisfies

$$\Big\| \sum_{\substack{m=1 \\ m \neq n}}^{N} \boldsymbol{G}(\boldsymbol{y}_n, \boldsymbol{y}_m; \omega) \boldsymbol{\alpha}(\boldsymbol{y}_m; \omega) \, \boldsymbol{E}_I(\boldsymbol{y}_m; \omega) \Big\| \ll \| \boldsymbol{E}_I(\boldsymbol{y}_n; \omega) \|.$$

Combining this approximation with (6) and (4), the total field at a receiver $\boldsymbol{x}_r \in \mathcal{A}$ becomes

$$\boldsymbol{E}(\boldsymbol{x}_r; \omega) = \boldsymbol{E}_I(\boldsymbol{x}_r; \omega) + \sum_{j=1}^{N} \boldsymbol{G}(\boldsymbol{x}_r, \boldsymbol{y}_n; \omega/c) \, \boldsymbol{\alpha}(\boldsymbol{y}_n) \, \boldsymbol{G}(\boldsymbol{y}_n, \boldsymbol{x}_s; \omega/c) \boldsymbol{j}_s(\omega).$$

Note, this approximation neglects all multiple scattering events. For strong multiple scattering, one can include higher order terms of the Born series [15], and/or use the Foldy-Lax model (see e.g, [19] for acoustics and [38] for electromagnetism).

2.1. The full data problem.
We first consider the ideal case where we measure all components of the total electric field at the array $\mathcal{A}$, corresponding to an illumination with an electric dipole source at $\boldsymbol{x}_s$ with known polarization vector $\boldsymbol{j}_s(\omega)$. Since different dipole moments $\boldsymbol{j}_s(\omega)$ could be used to control the incident field, one can extract from the measurements of the total field the array response function $\boldsymbol{\Pi}(\boldsymbol{x}_r, \boldsymbol{x}_s; k) \in \mathbb{C}^{3 \times 3}$ defined by

$$(7) \qquad \boldsymbol{\Pi}(\boldsymbol{x}_r, \boldsymbol{x}_s; k) = \sum_{n=1}^{N} \boldsymbol{G}(\boldsymbol{x}_r, \boldsymbol{y}_n; k) \, \boldsymbol{\alpha}(\boldsymbol{y}_n) \, \boldsymbol{G}(\boldsymbol{y}_n, \boldsymbol{x}_s; k), \ \forall \boldsymbol{x}_r \in \mathcal{A}.$$

2.2. Polarization data problem.
When working with light sources, it is hard to control all the components of the polarization vector $\boldsymbol{j}_s$ as we assumed in section 2.1. Actually only certain directions of the polarization vector matter. This is because the field $\boldsymbol{E}_I$ emanating from the electric dipole at $\boldsymbol{x}_s$ can be well approximated[1] in the vicinity of a point $\boldsymbol{y}_0$ far from $\boldsymbol{x}_s$ by the plane wave

$$(8) \qquad\qquad \boldsymbol{E}_I(\boldsymbol{x}; \omega) \approx \frac{\boldsymbol{p} \times \boldsymbol{k}}{|\boldsymbol{r}_0|} \exp[\imath \boldsymbol{k} \cdot \boldsymbol{x}],$$

with polarization $\boldsymbol{p} = (\boldsymbol{I} - \boldsymbol{r}_0 \boldsymbol{r}_0^T) \boldsymbol{j}_s$, wave vector $\boldsymbol{k} = k \boldsymbol{r}_0 / |\boldsymbol{r}_0|$ and $\boldsymbol{r}_0 = \boldsymbol{y}_0 - \boldsymbol{x}_s$. Thus if we are far away from a source, we may assume that only two orthogonal components of the polarization vector can be controlled, i.e. that $\boldsymbol{j}_s \in \mathrm{span}\{\boldsymbol{u}_1, \boldsymbol{u}_2\}$, where $\{\boldsymbol{u}_1, \boldsymbol{u}_2\}$ is a real orthonormal basis of polarization directions in $(\boldsymbol{y}_0 - \boldsymbol{x}_s)^\perp$, and $\boldsymbol{y}_0$ is a known and fixed point near the scatterers we wish to image. Instead of

---

[1]The plane wave approximation is rigorously justified in the asymptotic analysis of section 5.

assuming control of the phases and amplitudes of the vector $\boldsymbol{j}_s$, we assume it is a circularly symmetric Gaussian random vector (see e.g [33]) satisfying

$$(9) \qquad \langle \boldsymbol{j}_s \rangle = \boldsymbol{0}, \ \langle \boldsymbol{j}_s \boldsymbol{j}_s^* \rangle = \boldsymbol{J}_s = \boldsymbol{U}_s \widetilde{\boldsymbol{J}}_s \boldsymbol{U}_s^*, \ \text{and} \ \langle \boldsymbol{j}_s \boldsymbol{j}_s^T \rangle = \boldsymbol{0},$$

where $\boldsymbol{U}_s \equiv [\boldsymbol{u}_1, \boldsymbol{u}_2]$, $\boldsymbol{J}_s$ is a known 3×3 Hermitian matrix and $\langle \cdot \rangle$ denotes the mean or expectation. The assumptions on the frequency dependence of $\boldsymbol{j}_s$ are made later in section 6. Note that the 2×2 Hermitian matrix $\widetilde{\boldsymbol{J}}_s$ in (9) is the coherency matrix encoding the polarization state of the plane wave approximation near $\boldsymbol{y}_0$ of the point source with origin $\boldsymbol{x}_s$.

Similarly, if the array where we make measurements is far away from the scatterers, the scattered field can be approximated by a plane wave with polarization vector having a range component that is, for all practical purposes, zero (i.e. $\boldsymbol{p} \approx (p_1, p_2, 0)$). Thus the scattered field also has a range component that is very small compared to the cross-range components[2]. This motivates measuring the matrix of correlations between the cross-range components of the total electric field, i.e. the *coherency matrix* given by

$$(10) \qquad \boldsymbol{\Psi}(\boldsymbol{x}_r; \omega) := \boldsymbol{U}_\parallel^* \langle \boldsymbol{E}(\boldsymbol{x}_r; \omega) \boldsymbol{E}(\boldsymbol{x}_r; \omega)^* \rangle \boldsymbol{U}_\parallel,$$

where $\boldsymbol{U}_\parallel := [\boldsymbol{e}_1, \boldsymbol{e}_2]$. Assuming the source satisfies (9) and that the Born approximation holds, the coherency matrix becomes

$$
\begin{aligned}
(11) \qquad \boldsymbol{\Psi} &= \boldsymbol{U}_\parallel^* \langle (\boldsymbol{G} + \boldsymbol{\Pi}) \boldsymbol{j}_s \boldsymbol{j}_s^* (\boldsymbol{G} + \boldsymbol{\Pi})^* \rangle \boldsymbol{U}_\parallel \\
&= \boldsymbol{U}_\parallel^* (\boldsymbol{G} + \boldsymbol{\Pi}) \boldsymbol{U}_s \widetilde{\boldsymbol{J}}_s \boldsymbol{U}_s^* (\boldsymbol{G} + \boldsymbol{\Pi})^* \boldsymbol{U}_\parallel \\
&= \widetilde{\boldsymbol{G}} \widetilde{\boldsymbol{J}}_s \widetilde{\boldsymbol{G}}^* + \widetilde{\boldsymbol{\Pi}} \widetilde{\boldsymbol{J}}_s \widetilde{\boldsymbol{G}}^* + \widetilde{\boldsymbol{G}} \widetilde{\boldsymbol{J}}_s \widetilde{\boldsymbol{\Pi}}^* + \widetilde{\boldsymbol{\Pi}} \widetilde{\boldsymbol{J}}_s \widetilde{\boldsymbol{\Pi}}^*,
\end{aligned}
$$

where for clarity we dropped the dependence on the source, receiver and frequency, and we adopt the notation

$$(12) \qquad \widetilde{\boldsymbol{G}} = \boldsymbol{U}_\parallel^* \boldsymbol{G} \boldsymbol{U}_s \ \text{and} \ \widetilde{\boldsymbol{\Pi}} = \boldsymbol{U}_\parallel^* \boldsymbol{\Pi} \boldsymbol{U}_s.$$

3. Imaging method

The imaging method we present here is an electromagnetic adaptation of Kirchhoff migration (section 3.1). This method assumes the full data (as defined in section 2.1) is available. The strategy to image with polarization data is explained in section 3.2.

3.1. **Kirchhoff migration in electromagnetics.**
The single frequency electromagnetic version of the Kirchhoff imaging function that we use here comes from [18] and operates on a 3×3 complex matrix $\boldsymbol{\Pi}$ field defined on the array. For each point $\boldsymbol{y}$ in the imaging window, the imaging function produces a 3×3 complex matrix valued field given by

$$(13) \qquad \mathcal{I}_{KM}[\boldsymbol{\Pi}](\boldsymbol{y}; k) = \int_{\mathcal{A}} d\boldsymbol{x}_{r,\parallel} \, \overline{\boldsymbol{G}(\boldsymbol{x}_r, \boldsymbol{y}; k)} \, \boldsymbol{\Pi}(\boldsymbol{x}_r, \boldsymbol{x}_s; k) \, \overline{\boldsymbol{G}(\boldsymbol{x}_s, \boldsymbol{y}; k)},$$

where the integral is done with respect to the cross-range coordinates $\boldsymbol{x}_{r,\parallel}$, and with a slight abuse of notation $\mathcal{A}$ denotes the set representing the planar array $\mathcal{A}$.

---

[2]This is rigorously justified by the Fraunhofer regime asymptotic study of section 5.

When the data $\boldsymbol{\Pi}$ comes from N point-like scatterers (7), the Kirchhoff image can be written explicitly as

(14)
$$\mathcal{I}_{KM}[\boldsymbol{\Pi}](\boldsymbol{y};k)$$
$$= \sum_{n=1}^{N} \left[\int_{\mathcal{A}} d\boldsymbol{x}_{r,\parallel} \, \overline{\boldsymbol{G}\left(\boldsymbol{x}_r,\boldsymbol{y};k\right)} \boldsymbol{G}\left(\boldsymbol{x}_r,\boldsymbol{y}_n;k\right) \right] \boldsymbol{\alpha}(\boldsymbol{y}_n) \, \boldsymbol{G}\left(\boldsymbol{y}_n,\boldsymbol{x}_s;k\right) \, \overline{\boldsymbol{G}\left(\boldsymbol{x}_s,\boldsymbol{y};k\right)}$$
$$= \sum_{n=1}^{N} \boldsymbol{H}_r\left(\boldsymbol{y},\boldsymbol{y}_n;k\right) \, \boldsymbol{\alpha}(\boldsymbol{y}_n) \, \boldsymbol{H}_s\left(\boldsymbol{y},\boldsymbol{y}_n;k\right)^{\top},$$

where $\boldsymbol{H}_s$ and $\boldsymbol{H}_r$ are the 3×3 complex symmetric matrices defined by:

(15)
$$\boldsymbol{H}_s(\boldsymbol{y},\boldsymbol{y}';k) = \overline{\boldsymbol{G}\left(\boldsymbol{x}_s,\boldsymbol{y};k\right)} \, \boldsymbol{G}(\boldsymbol{x}_s,\boldsymbol{y}';k) \text{ and}$$
$$\boldsymbol{H}_r\left(\boldsymbol{y},\boldsymbol{y}';k\right) = \int_{\mathcal{A}} d\boldsymbol{x}_{r,\parallel} \, \overline{\boldsymbol{G}\left(\boldsymbol{x}_r,\boldsymbol{y};k\right)} \boldsymbol{G}\left(\boldsymbol{x}_r,\boldsymbol{y}';k\right).$$

3.2. **Strategy for imaging with polarization data.** Our imaging method consists of two steps. The first step is "preprocessing" the coherency matrix data (11) to estimate the cross-range components of the full data (7). The second step is using Kirchhoff migration to image using this preprocessed data. We prove that the error made in the preprocessing step does not appear in the Kirchhoff image, and thus the image we get with coherency matrix data is (asymptotically) identical to the image we would obtain with full data (see the stationary phase argument in section 4). If $\boldsymbol{\Psi}$ is the 2×2 complex Hermitian matrix representing the coherency matrix, the preprocessing is defined by the mapping $\boldsymbol{p}$ that takes a 2×2 matrix field in the array and gives the 3×3 matrix field given by

(16)
$$\boldsymbol{p}(\boldsymbol{\Psi}) := \boldsymbol{U}_{\parallel}[\boldsymbol{\Psi} - \widetilde{\boldsymbol{G}}\widetilde{\boldsymbol{J}}_s\widetilde{\boldsymbol{G}}^*]\widetilde{\boldsymbol{G}}^{-*}\widetilde{\boldsymbol{J}}_s^{-1}\boldsymbol{U}_s^*,$$

where we omitted the dependency on source, receiver and frequency of $\boldsymbol{\Psi}$ and $\widetilde{\boldsymbol{G}}$ (the 2×2 submatrix of $\boldsymbol{G}$ defined in (12)). The preprocessing map is designed to extract the 2×2 submatrix $\widetilde{\boldsymbol{\Pi}}$ of $\boldsymbol{\Pi}$ from the coherency matrix data $\boldsymbol{\Psi}$. Indeed, applying the preprocessing $\boldsymbol{p}$ to the data (11) we get

(17)
$$\boldsymbol{p}(\boldsymbol{\Psi}) = \boldsymbol{U}_{\parallel}\widetilde{\boldsymbol{\Pi}}\boldsymbol{U}_s^* + \boldsymbol{q},$$

where the error $\boldsymbol{q}$ includes antilinear and sesquilinear terms in $\widetilde{\boldsymbol{\Pi}}$:

(18)
$$\boldsymbol{q} := \boldsymbol{U}_{\parallel}[\widetilde{\boldsymbol{G}}\widetilde{\boldsymbol{J}}_s\widetilde{\boldsymbol{\Pi}}^* + \widetilde{\boldsymbol{\Pi}}\widetilde{\boldsymbol{J}}_s\widetilde{\boldsymbol{\Pi}}^*]\widetilde{\boldsymbol{G}}^{-*}\widetilde{\boldsymbol{J}}_s^{-1}\boldsymbol{U}_s^*.$$

We prove later in section 5.7 that it is possible to image with $\boldsymbol{U}_{\parallel}\widetilde{\boldsymbol{\Pi}}\boldsymbol{U}_s^*$ instead of $\boldsymbol{\Pi}$. Finally note that the preprocessing requires to calculate the inverse of the 2×2 matrix $\widetilde{\boldsymbol{G}}^*$ for every point of the array. This matrix is in general invertible, with a condition number depending only the relative positions of the array, the source and the scatterers, as is proved in appendix B. We also assume invertibility of the coherency matrix $\widetilde{\boldsymbol{J}}_s$ of the source. This can be guaranteed by doing two experiments with different source polarizations (e.g. two orthogonal linear polarizations) or by considering a source with sufficiently rich polarizations.

4. Kirchhoff imaging of preprocessed coherency matrix

We now use a stationary phase argument to show that the Kirchhoff image of the preprocessed coherency matrix (10) for a collection of point scatterers is asymptotically close to the Kirchhoff image (7) obtained in the same experimental setup by assuming that one can measure the corresponding field components with the data $\boldsymbol{U}_\parallel \widetilde{\boldsymbol{\Pi}} \boldsymbol{U}_s^*$. Thus, the missing phase information in the data $\boldsymbol{p}(\boldsymbol{\Psi})$ does not affect the Kirchhoff image when the frequency is sufficiently high. In the following, the box $\mathcal{W} = [-b/2, b/2]^2 \times [L - h/2, L + h/2]$ is the imaging window that is assumed to contain all the scatterers. For simplicity we also assume that $\boldsymbol{\alpha}$ and $\boldsymbol{J}_s$ are constant in frequency. This assumption can be easily relaxed to include smooth frequency dependence provided the growth of these quantities (and all their derivatives) as $\omega \to \infty$ is dominated by a polynomial.
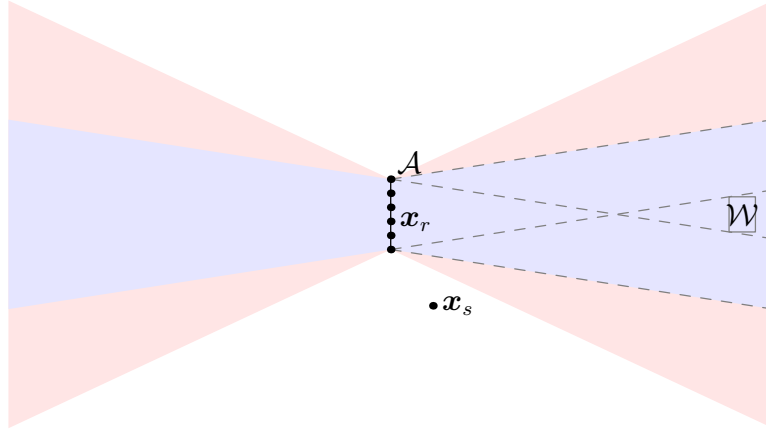

FIGURE 2. In theorem 1, the source $\boldsymbol{x}_s$ needs to be outside of the region $\mathcal{R}(\gamma)$ given in (20). A two dimensional example of $\mathcal{R}(1)$ is given in light blue and is constructed by taking the union of identical cones with tips at the array. The cones are sufficiently wide so that each one contains the imaging window. The positive part of the cones with tip at the boundary of the array are in dashed line. The light red areas need to be added to deal with multiple scattering, where the region should be $\mathcal{R}(3)$.

Theorem 1. *For all points $\boldsymbol{y}$ in the imaging window $\mathcal{W}$ we have*

$$(19) \qquad \mathcal{I}_{KM}[\boldsymbol{p}(\boldsymbol{\Psi})](\boldsymbol{y}; k) = \mathcal{I}_{KM}[\boldsymbol{U}_\parallel \widetilde{\boldsymbol{\Pi}} \boldsymbol{U}_s^*](\boldsymbol{y}; k) + o(1), \ as \ k \to \infty,$$

the source location $\boldsymbol{x}_s$ is outside *of the region $\mathcal{R}(\gamma)$ defined by*

$$(20) \qquad \mathcal{R}(\gamma) = \bigcup_{\boldsymbol{x}_r \in \mathcal{A}} \left\{ \boldsymbol{y} \mid |\boldsymbol{x}_{r,\parallel} - \boldsymbol{y}_\parallel| \le c\gamma |\boldsymbol{x}_r - \boldsymbol{y}| \right\},$$

where

$$(21) \qquad c = \frac{a + b}{\sqrt{(2L - h)^2 + (a + b)^2}}.$$

If weak scattering holds (i.e. Born approximation) we can take $\gamma = 1$. Alternatively, if finitely many scattering events are kept, $\gamma = 3$ is sufficient. See fig. 2 for a visualization of the region $\mathcal{R}(\gamma)$ for different γ.

Proof. We recall from (17) that the preprocessing of the coherency matrix data $\boldsymbol{\Psi}$ gives $\boldsymbol{U}_\| \widetilde{\boldsymbol{\Pi}} \boldsymbol{U}_s^*$ plus the error $\boldsymbol{q}$ given in (18). Hence it suffices to show that

$$(22) \qquad \mathcal{I}_{KM}[\boldsymbol{q}; k](\boldsymbol{y}) \to 0, \text{ as } k \to \infty.$$

To show how to handle multiple scattering, we use the second Born approximation. Higher order (but finite) Born approximations can be considered with identical hypothesis. We assume the scattered field is $\boldsymbol{\Pi} = \boldsymbol{\Pi}_1 + \boldsymbol{\Pi}_2$ where $\boldsymbol{\Pi}_1$ (resp. $\boldsymbol{\Pi}_2$) consists of single (resp. double) scattering events. From (6) $\boldsymbol{\Pi}_2$ is given by

$$(23)$$
$$\boldsymbol{\Pi}_2(\boldsymbol{x}_r, \boldsymbol{x}_s; k) = \sum_{n,m,m \neq n} \boldsymbol{G}(\boldsymbol{x}_r, \boldsymbol{y}_n; k)\, \boldsymbol{\alpha}(\boldsymbol{y}_n)\, \boldsymbol{G}(\boldsymbol{y}_n, \boldsymbol{y}_m; k)\, \boldsymbol{\alpha}(\boldsymbol{y}_m)\, \boldsymbol{G}(\boldsymbol{y}_m, \boldsymbol{x}_s; k).$$

The preprocessing error (18) is the sum of the terms

$$(24) \quad \boldsymbol{q}_j = \boldsymbol{U}_\| \widetilde{\boldsymbol{G}} \widetilde{\boldsymbol{J}}_s \widetilde{\boldsymbol{\Pi}}_j^* \widetilde{\boldsymbol{G}}^{-*} \widetilde{\boldsymbol{J}}_s^{-1} \boldsymbol{U}_s^* \text{ and } \boldsymbol{q}_{i,j} = \boldsymbol{U}_\| \widetilde{\boldsymbol{\Pi}}_i \widetilde{\boldsymbol{J}}_s \widetilde{\boldsymbol{\Pi}}_j^* \widetilde{\boldsymbol{G}}^{-*} \widetilde{\boldsymbol{J}}_s^{-1} \boldsymbol{U}_s^*, \; i, j = 1, 2.$$

Error term $\boldsymbol{q}_1$: The Kirchhoff image of $\boldsymbol{q}_1$ is a sum of oscillatory integrals of the form

$$(25) \qquad \int d\boldsymbol{x}_{r,\|} \boldsymbol{C}(\boldsymbol{x}_r, \boldsymbol{x}_s; k) \exp[\imath k \phi(\boldsymbol{x}_r, \boldsymbol{y})],$$

where the phase is

$$(26) \qquad \phi(\boldsymbol{x}_r, \boldsymbol{y}) = 2|\boldsymbol{x}_r - \boldsymbol{x}_s| - |\boldsymbol{x}_r - \boldsymbol{y}_*| - |\boldsymbol{x}_s - \boldsymbol{y}_*| - |\boldsymbol{x}_r - \boldsymbol{y}| - |\boldsymbol{x}_s - \boldsymbol{y}|,$$

where $\boldsymbol{y}_* \in \mathcal{W}$ is one of scatterers and $\boldsymbol{C}(\boldsymbol{x}_r, \boldsymbol{x}_s; k)$ is a complex symmetric matrix that is smooth for $\boldsymbol{x}_r \in \mathcal{A}$ and is supported in $\mathcal{A}$ (as a function of $\boldsymbol{x}_r$). We make this assumption to ignore any boundary terms arising from the stationary phase method. The "amplitude" matrix $\boldsymbol{C}(\boldsymbol{x}_r, \boldsymbol{x}_s; k)$ can be expanded as a power series for $k \neq 0$:

$$(27) \qquad \boldsymbol{C}(\boldsymbol{x}_r, \boldsymbol{x}_s; k) = \sum_{j=0}^\infty k^{-j} \boldsymbol{C}_j(\boldsymbol{x}_r, \boldsymbol{x}_s),$$

uniformly for $\boldsymbol{x}_r \in \mathcal{A}$. The matrix valued terms $\boldsymbol{C}_j(\boldsymbol{x}_r, \boldsymbol{x}_s)$ are independent of k and are smooth in $\boldsymbol{x}_r$ because $\boldsymbol{x}_r \neq \boldsymbol{x}_s$. Their explicit expression does not matter for the argument. We can apply the stationary phase method to approximate (25) because $\boldsymbol{C}(\boldsymbol{x}_r, \boldsymbol{x}_s; k)$ and all its derivatives with respect to $\boldsymbol{x}_{r,\|}$ are bounded as $k \to \infty$ (see e.g. [25]). We deduce that $\mathcal{I}_{KM}[\boldsymbol{q}_1](\boldsymbol{y}) \to 0$ as $k \to \infty$ provided there are no points $\boldsymbol{x}_r \in \mathcal{A}$ for which the phase (26) is stationary, i.e. there are no points $\boldsymbol{x}_r \in \mathcal{A}$ such that the gradient

$$(28) \qquad \nabla_{\boldsymbol{x}_{r,\|}} \phi = 2\frac{\boldsymbol{x}_{r,\|} - \boldsymbol{x}_{s,\|}}{|\boldsymbol{x}_r - \boldsymbol{x}_s|} - \frac{\boldsymbol{x}_{r,\|} - \boldsymbol{y}_{*,\|}}{|\boldsymbol{x}_r - \boldsymbol{y}_*|} - \frac{\boldsymbol{x}_{r,\|} - \boldsymbol{y}_\|}{|\boldsymbol{x}_r - \boldsymbol{y}|},$$

vanishes. To guarantee there are no stationary points[3], we use the known positions of the array and the imaging window to define the region $\mathcal{R}(1)$ in (20) as a union for $\boldsymbol{x}_r \in \mathcal{A}$ of the cones $\{\boldsymbol{y} \mid |\boldsymbol{x}_{r,\|} - \boldsymbol{y}_\|| \leq c|\boldsymbol{x}_r - \boldsymbol{y}|\}$, where c is chosen so that each cone contains the imaging window $\mathcal{W}$ and is given by (21), see fig. 2. The

---

[3]The stationary argument we use here corrects the similar one used in [9], which has a region $\mathcal{R}$ that may be too small.

expression (21) comes from an elementary geometric argument involving the cones with tips at the boundary of the array (in dashed line in fig. 2). If $\boldsymbol{x}_r$ is a stationary point then there are points $\boldsymbol{y}, \boldsymbol{y}_* \in \mathcal{W}$ for which (28) is zero. Isolating the term corresponding to $\boldsymbol{x}_s$ and taking norms we get

$$(29) \qquad 2\frac{|\boldsymbol{x}_{r,\|} - \boldsymbol{x}_{s,\|}|}{|\boldsymbol{x}_r - \boldsymbol{x}_s|} \leq \frac{|\boldsymbol{x}_{r,\|} - \boldsymbol{y}_{*,\|}|}{|\boldsymbol{x}_r - \boldsymbol{y}_*|} + \frac{|\boldsymbol{x}_{r,\|} - \boldsymbol{y}_{\|}|}{|\boldsymbol{x}_r - \boldsymbol{y}|} \leq 2c,$$

where the last inequality follows from $\boldsymbol{y}, \boldsymbol{y}_* \in \mathcal{W} \subset \mathcal{R}(1)$. We conclude that $\boldsymbol{x}_s \in \mathcal{R}(1)$. To summarize, if $\boldsymbol{x}_s \notin \mathcal{R}(1)$, the Kirchhoff image of $\boldsymbol{q}_1$ vanishes as $k \to \infty$ (faster than any polynomial in k^{-1}).

Weak scattering assumption: If we operate under the weak scattering assumption, we are done since we can neglect $\boldsymbol{q}_2$, $\boldsymbol{q}_{i,j}$ and $\boldsymbol{\Pi}_1 \boldsymbol{\Pi}_1^*$.

Error term $\boldsymbol{q}_2$: The term $\boldsymbol{q}_2$ is composed of oscillatory integrals of the form (25) but with phase given by

$$(30) \quad \phi(\boldsymbol{x}_r, \boldsymbol{y}) = 2|\boldsymbol{x}_r - \boldsymbol{x}_s| - |\boldsymbol{x}_r - \boldsymbol{y}_n| - |\boldsymbol{y}_n - \boldsymbol{y}_m| - |\boldsymbol{y}_m - \boldsymbol{x}_s| - |\boldsymbol{x}_r - \boldsymbol{y}| - |\boldsymbol{y} - \boldsymbol{x}_s|.$$

The gradient of (30) with respect to $\boldsymbol{x}_{r,\|}$ is given by

$$(31) \qquad \nabla_{\boldsymbol{x}_{r,\|}} \phi = 2\frac{\boldsymbol{x}_{r,\|} - \boldsymbol{x}_{s,\|}}{|\boldsymbol{x}_r - \boldsymbol{x}_s|} - \frac{\boldsymbol{x}_{r,\|} - \boldsymbol{y}_{n,\|}}{|\boldsymbol{x}_r - \boldsymbol{y}_n|} - \frac{\boldsymbol{x}_{r,\|} - \boldsymbol{y}_{\|}}{|\boldsymbol{x}_r - \boldsymbol{y}|}.$$

If there are points $\boldsymbol{y}_n, \boldsymbol{y} \in \mathcal{W} \subset \mathcal{R}(1)$ such that $\nabla_{\boldsymbol{x}_{r,\|}} \phi = 0$, we can conclude in a way similar to (29) that $\boldsymbol{x}_s \in \mathcal{R}(1)$. Taking $\boldsymbol{x}_s \notin \mathcal{R}(1)$ guarantees that there are no stationary phase points.

Error term $\boldsymbol{q}_{i,j}$: This term is composed of oscillatory integrals of the form (25) with phase

$$(32) \qquad \phi(\boldsymbol{x}_r, \boldsymbol{y}) = |\boldsymbol{x}_r - \boldsymbol{x}_s| + \phi_i - \phi_j' - |\boldsymbol{x}_r - \boldsymbol{y}| - |\boldsymbol{x}_s - \boldsymbol{y}|, \ i,j = 1,2$$

where $\phi_1 = |\boldsymbol{x}_r - \boldsymbol{y}_m| + |\boldsymbol{y}_m - \boldsymbol{x}_s|$, $\phi_2 = |\boldsymbol{x}_r - \boldsymbol{y}_m| + |\boldsymbol{y}_m - \boldsymbol{y}_n| + |\boldsymbol{y}_n - \boldsymbol{x}_s|$, and $m \neq n$ are scatterer indices. By ϕ_j' we mean putting on the indices n and m, to represent taking a possibly different path among the scatterers. Its gradient with respect to $\boldsymbol{x}_{r,\|}$ is

$$(33) \qquad \nabla_{\boldsymbol{x}_{r,\|}} \phi = \frac{\boldsymbol{x}_{r,\|} - \boldsymbol{x}_{s,\|}}{|\boldsymbol{x}_r - \boldsymbol{x}_s|} + \frac{\boldsymbol{x}_{r,\|} - \boldsymbol{y}_{m,\|}}{|\boldsymbol{x}_r - \boldsymbol{y}_m|} - \frac{\boldsymbol{x}_{r,\|} - \boldsymbol{y}_{m',\|}}{|\boldsymbol{x}_r - \boldsymbol{y}_{m'}|} - \frac{\boldsymbol{x}_{r,\|} - \boldsymbol{y}_{\|}}{|\boldsymbol{x}_r - \boldsymbol{y}|}.$$

If there are points $\boldsymbol{y}_m, \boldsymbol{y}_{m'}, \boldsymbol{y} \in \mathcal{W} \subset \mathcal{R}(1)$ such that $\nabla_{\boldsymbol{x}_{r,\|}} \phi = 0$ then proceeding as in (29) we get

$$(34) \qquad \frac{|\boldsymbol{x}_{r,\|} - \boldsymbol{x}_{s,\|}|}{|\boldsymbol{x}_r - \boldsymbol{x}_s|} \leq \frac{|\boldsymbol{x}_{r,\|} - \boldsymbol{y}_{m,\|}|}{|\boldsymbol{x}_r - \boldsymbol{y}_m|} + \frac{|\boldsymbol{x}_{r,\|} - \boldsymbol{y}_{m',\|}|}{|\boldsymbol{x}_r - \boldsymbol{y}_{m'}|} + \frac{|\boldsymbol{x}_{r,\|} - \boldsymbol{y}_{\|}|}{|\boldsymbol{x}_r - \boldsymbol{y}|} \leq 3c.$$

We conclude $\boldsymbol{x}_s \in \mathcal{R}(3)$ and that taking $\boldsymbol{x}_s \notin \mathcal{R}(3)$ guarantees the absence of stationary points. $\qquad \square$

Remark 1. *Let us call $\boldsymbol{q}_j$ the antilinear term involving the $j-$th term in the Born series and $\boldsymbol{q}_{i,j}$ the sesquilinear term involving the $i-$th and $j-$th terms. Clearly $\nabla_{\boldsymbol{x}_{r,\|}} \boldsymbol{q}_j$ is of the form (28) and $\nabla_{\boldsymbol{x}_{r,\|}} \boldsymbol{q}_{i,j}$ is of the form (33). This is because for any path going from $\boldsymbol{x}_r$, going through a chain of scatterers and then to $\boldsymbol{x}_s$, there is only one segment involving $\boldsymbol{x}_r$. Hence the proof of theorem 1 can be modified to include these higher order terms.*
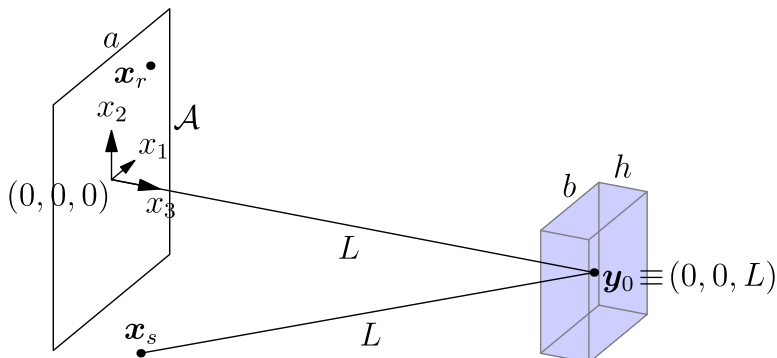
FIGURE 3. Fraunhofer regime scalings. The array $\mathcal{A}$ has side a and lies in the x_1, x_2 plane and the imaging window is a box of dimensions b in cross-range and h in range. The point $\boldsymbol{y}_0 = (0, 0, L)$ is the reference point for the imaging window. The source $\boldsymbol{x}_s$ is not in the array and $|\boldsymbol{x}_s - \boldsymbol{y}_0| = L$.

Remark 2. *The region $\mathcal{R}(\gamma)$ that we have to avoid for placing the source in theorem 1 is a worst case scenario that assumes no knowledge about the position of the scatterers, other than them being in $\mathcal{W}$. This exclusion region can be smaller since the scatterers are point-like.*

Remark 3. *Notice that in the proof of theorem 1, all the phase terms of the error in the Kirchhoff imaging function never vanish. This is not the case for the phase of the oscillatory integral appearing in the image $\mathcal{I}_{KM}(\boldsymbol{U}_{\|}\widetilde{\boldsymbol{\Pi}}\boldsymbol{U}_s^*)$. This is essentially the travel time argument that can be used to motivate Kirchhoff image (see [11]). In the next section we do a resolution analysis of the Kirchhoff imaging function, i.e. characterizing the typical size of a focal spot (in both range and cross-range).*

5. FRAUNHOFER ASYMPTOTIC ANALYSIS

We begin the study of the Kirchhoff imaging function in the Fraunhofer diffraction regime by giving the assumptions we make about the length scales of the problem for both the array (section 5.1) and the source (section 5.2). Under these assumptions, we give expressions for the data and the imaging function (section 5.3) that allow us to get resolution estimates in both cross-range (i.e. plane parallel to the array, see section 5.4) and range (i.e. direction normal to the array, see section 5.5). Extracting the polarizability tensor data from the Kirchhoff images gives oscillatory artifacts that we correct in section 5.6. Finally we explain in section 5.7 why it is possible to image with the full data projected on an appropriate basis.

5.1. **Length scales for Fraunhofer asymptotic regime.** Let $\boldsymbol{y} = (\boldsymbol{y}_{\|}, L + \eta)$ and $\boldsymbol{x}_r = (\boldsymbol{x}_{r,\|}, 0)$ be respectively an imaging point and a point in the array, with L being the characteristic propagation distance. We assume that the scatterers lie in a known imaging window of characteristic size b in cross-range and h in range, i.e. $|\boldsymbol{y}_{\|}| = \mathcal{O}(b)$ and $|\eta| = \mathcal{O}(h)$, as illustrated in fig. 3. For the Fraunhofer asymptotic regime we assume the following scalings hold (see e.g. [13, 15]).

- $kL \gg 1$, (high frequency or large propagation distance)

- Fresnel number $\Theta_a \equiv \dfrac{ka^2}{L} \ll kL$, i.e. small aperture: $a \ll L$,
- Fresnel number $\Theta_b \equiv \dfrac{kb^2}{L} \ll kL$, i.e. small imaging window in cross-range: $b \ll L$,
- Fresnel number $\Theta_h \equiv \dfrac{kh^2}{L} \ll kL$, i.e. small imaging window in range $h \ll L$.

Moreover we assume that

$$\Theta_b \ll 1, \ 1 \ll \Theta_a \ll \frac{L^2}{a^2}, \ \text{and } kh = \mathcal{O}(1),$$

namely that the imaging window is small compared to the array aperture (i.e. $b \ll a$) and that the range component η of the imaging point is small or of the order of the wavelength $2\pi/k$.

5.2. Asymptotic analysis related to the source.
Let $\boldsymbol{y}_0 \equiv (0,0,L)$ be a reference point in the imaging window. We assume for simplicity that the source-to-scatterer and array-to-scatterer distances are identical, i.e. $|\boldsymbol{x}_s - \boldsymbol{y}_0| = L$. Nevertheless, all the asymptotic results we present here hold if L and $|\boldsymbol{x}_s - \boldsymbol{y}_0|$ have the same order of magnitude. With this assumption, it is easy to check that the distance between the source $\boldsymbol{x}_s$ and an imaging point $\boldsymbol{y}$ satisfies:

$$(35) \qquad |\boldsymbol{y} - \boldsymbol{x}_s| = L\Big[1 + \mathcal{O}\Big(\frac{b}{L}\Big) + \mathcal{O}\Big(\frac{h}{L}\Big)\Big].$$

5.3. Fraunhofer asymptotic analysis of the Kirchhoff imaging function.
In the Fraunhofer regime (see[18, eq. (8)]), the dyadic Green function between an imaging point $\boldsymbol{y}$ and a receiver $\boldsymbol{x}_r$ on the array is given by

$$(36) \qquad \boldsymbol{G}(\boldsymbol{x}_r, \boldsymbol{y}; k) \ = \ \widetilde{G}(\boldsymbol{x}_r, \boldsymbol{y}; k)\Big[\boldsymbol{P}(\boldsymbol{x}_r, \boldsymbol{y}) + \mathcal{O}\Big(\frac{a^2\Theta_a}{L^2}\Big) + \mathcal{O}(\Theta_b)\Big],$$

where $\widetilde{G}(\boldsymbol{x}_r, \boldsymbol{y}; k)$ is the Fraunhofer or paraxial approximation of the acoustic Green function:

$$\widetilde{G}(\boldsymbol{x}_r, \boldsymbol{y}; k) \equiv \frac{1}{4\pi L} \ \exp\Big[\imath\Big(kL + \frac{k|\boldsymbol{x}_r|^2}{2L} + \frac{k\boldsymbol{x}_{r,\|} \cdot \boldsymbol{y}_\|}{L} + k\eta\Big)\Big],$$

and $\boldsymbol{P}(\boldsymbol{x}, \boldsymbol{y})$ is the orthogonal projector defined by

$$\boldsymbol{P}(\boldsymbol{x}, \boldsymbol{y}) = \boldsymbol{I} - \frac{(\boldsymbol{x} - \boldsymbol{y})(\boldsymbol{x} - \boldsymbol{y})^\top}{|\boldsymbol{x} - \boldsymbol{y}|^2},$$

with $\boldsymbol{I}$ being the 3×3 identity matrix. For convenience we introduce two particular projectors: the projector $\boldsymbol{P}_\|$ on the cross-range direction of $\mathcal{A}$ and the projector $\boldsymbol{P}_s$ on $(\boldsymbol{y}_0 - \boldsymbol{x}_s)^\perp$. We write these projectors in terms of an orthonormal basis of their range

$$(37) \qquad \boldsymbol{P}_\| = \boldsymbol{U}_\| \boldsymbol{U}_\|^* \ \text{and} \ \boldsymbol{P}_s = \boldsymbol{P}(\boldsymbol{x}_s, \boldsymbol{y}_0) = \boldsymbol{U}_s \boldsymbol{U}_s^*,$$

where $\boldsymbol{U}_\| \equiv [\boldsymbol{e}_1, \boldsymbol{e}_2]$ is a 3×2 matrix and the columns of the 3×2 matrix $\boldsymbol{U}_s$ form an orthonormal basis of $(\boldsymbol{y}_0 - \boldsymbol{x}_s)^\perp$, that we assume is chosen a priori.

In this regime, the projector $\boldsymbol{P}(\boldsymbol{x}_r, \boldsymbol{y})$ can be approximated by

$$(38) \qquad \boldsymbol{P}(\boldsymbol{x}_r, \boldsymbol{y}) = \boldsymbol{P}_\| + \mathcal{O}\Big(\frac{a}{L}\Big),$$

since $b = o(a)$, $\mathcal{O}(h/L) = \mathcal{O}(1/kL) = \mathcal{O}(a^2/(L^2\Theta_a)) = o(a^2/L^2)$ and $|\boldsymbol{x}_r - \boldsymbol{y}|^{-2} = L^{-2}(1 + \mathcal{O}(a^2/L^2))$. Thus, relation (36) simplifies to:

$$(39) \qquad \boldsymbol{G}(\boldsymbol{x}_r, \boldsymbol{y}; k) = \widetilde{G}(\boldsymbol{x}_r, \boldsymbol{y}; k)\Big[\boldsymbol{P}_\| + \mathcal{O}\Big(\frac{a^2\Theta_a}{L^2}\Big) + \mathcal{O}(\Theta_b) + \mathcal{O}\Big(\frac{a}{L}\Big)\Big].$$

Now, it follows by using (39) and integrating on the array that the matrix $\boldsymbol{H}_r\,(\boldsymbol{y}, \boldsymbol{y}_n; k)$ (defined in (15)) admits the following asymptotic expansion:

$$(40) \qquad \boldsymbol{H}_r\,(\boldsymbol{y}, \boldsymbol{y}_n; k) = \widetilde{\boldsymbol{H}}_r\,(\boldsymbol{y}, \boldsymbol{y}_n; k) + \mathcal{O}\Big(\frac{a^4\Theta_a}{L^4}\Big) + \mathcal{O}\Big(\frac{a^2\Theta_b}{L^2}\Big) + \Big(\frac{a^3}{L^3}\Big),$$

where for $\boldsymbol{y} = (\boldsymbol{y}_\|, L + \eta)$ and $\boldsymbol{y}' = (\boldsymbol{y}'_\|, L + \eta')$, $\widetilde{\boldsymbol{H}}_r\,(\boldsymbol{y}, \boldsymbol{y}'; k)$ is given by

$$\widetilde{\boldsymbol{H}}_r\,(\boldsymbol{y}, \boldsymbol{y}'; k) \;\; = \;\; \frac{\exp[\imath k(\eta' - \eta)]}{(4\pi L)^2}\int_{\mathcal{A}} d\boldsymbol{x}_{r,\|}\,\exp\Big[\imath k\Big(\frac{\boldsymbol{x}_{r,\|} \cdot (\boldsymbol{y}'_\| - \boldsymbol{y}_\|)}{L}\Big)\Big]\,\boldsymbol{P}_\|$$

$$(41) \qquad\qquad = \;\; \frac{\exp[\imath k(\eta' - \eta)]}{(4\pi L)^2}\,\mathcal{F}[\mathbb{1}_{\mathcal{A}}]\Big(\frac{k}{L}(\boldsymbol{y}'_\| - \boldsymbol{y}_\|)\Big)\boldsymbol{P}_\|.$$

Here $\mathbb{1}_{\mathcal{A}}$ denotes the indicator function of the array and $\mathcal{F}[f]$ is the Fourier transform of an integrable function f, defined using the convention

$$\mathcal{F}[f](\boldsymbol{\xi}_\|) = \int_{\mathbb{R}^2} f(\boldsymbol{x}_\|)\exp[\imath\boldsymbol{x}_\| \cdot \boldsymbol{\xi}_\|]\,d\boldsymbol{x}_\|, \;\; \forall f \in L^1(\mathbb{R}^2).$$

The dyadic Green function between an imaging point $\boldsymbol{y}$ and the source has asymptotic expansion [18, eq. (7)]

$$(42) \qquad\qquad \boldsymbol{G}(\boldsymbol{x}_s, \boldsymbol{y}; k) = G(\boldsymbol{x}_s, \boldsymbol{y}; k)\Big[\boldsymbol{P}(\boldsymbol{x}_s, \boldsymbol{y}) + \mathcal{O}\Big(\frac{1}{kL}\Big)\Big].$$

One can also show using (35) that the projector $\boldsymbol{P}(\boldsymbol{x}_s, \boldsymbol{y})$ can be approximated in the Fraunhofer regime by

$$(43) \qquad\qquad \boldsymbol{P}(\boldsymbol{x}_s, \boldsymbol{y}) = \boldsymbol{P}_s + \mathcal{O}\Big(\frac{b}{L}\Big) + \mathcal{O}\Big(\frac{h}{L}\Big).$$

Using (42), (35) and (43) we get that

$$\boldsymbol{G}(\boldsymbol{x}_s, \boldsymbol{y}; k) \;\; = \;\; \frac{e^{\imath k|\boldsymbol{x}_s - \boldsymbol{y}|}}{4\pi L}\Big[1 + \mathcal{O}\Big(\frac{b}{L}\Big) + \mathcal{O}\Big(\frac{h}{L}\Big)\Big]\Big[\boldsymbol{P}_s + \mathcal{O}\Big(\frac{b}{L}\Big) + \mathcal{O}\Big(\frac{1}{k\,L}\Big)\Big]$$

$$(44) \qquad\qquad = \;\; \frac{e^{\imath k|\boldsymbol{x}_s - \boldsymbol{y}|}}{4\pi L}\Big[\boldsymbol{P}_s + O\Big(\frac{b}{L}\Big) + \mathcal{O}\Big(\frac{a^2}{\Theta_a L^2}\Big)\Big],$$

since $kh = \mathcal{O}(1)$ implies that $\mathcal{O}(h/L) = \mathcal{O}\,(1/(kL)) = \mathcal{O}\,(a^2/(\Theta_a L^2))$. Thus, the matrix $\boldsymbol{H}_s\,(\boldsymbol{y}, \boldsymbol{y}_n; k)$ admits the asymptotic expansion:

$$(45) \qquad \boldsymbol{H}_s\,(\boldsymbol{y}, \boldsymbol{y}_n; k) = \frac{1}{(4\pi L)^2}\Big[\widetilde{\boldsymbol{H}}_s\,(\boldsymbol{y}, \boldsymbol{y}_n; k) + O\Big(\frac{b}{L}\Big) + \mathcal{O}\Big(\frac{a^2}{\Theta_a L^2}\Big)\Big],$$

where for $\boldsymbol{y} = (\boldsymbol{y}_\|, L + \eta)$ and $\boldsymbol{y}' = (\boldsymbol{y}'_\|, L + \eta')$:

$$(46) \qquad\qquad \widetilde{\boldsymbol{H}}_s\,(\boldsymbol{y}, \boldsymbol{y}'; k) = \exp\left[\imath k(|\boldsymbol{x}_s - \boldsymbol{y}'| - |\boldsymbol{x}_s - \boldsymbol{y}|)\right]\boldsymbol{P}_s.$$

We assume from now on that all polarizability tensors have the same order of magnitude and that $\|\boldsymbol{\alpha}_n\| = \mathcal{O}(1)$ for $n = 1, \ldots, N$. The main result of this section is the following asymptotic expansion.

Proposition 1. *The Kirchhoff imaging function applied to full array data from N scatterers admits the asymptotic expansion*

$$\mathcal{I}_{KM}(\boldsymbol{y};k) = \frac{1}{(4\pi L)^2}\left[\sum_{n=1}^{N}\widetilde{\boldsymbol{H}}_r\left(\boldsymbol{y},\boldsymbol{y}_n;k\right)\boldsymbol{\alpha}(\boldsymbol{y}_n)\,\widetilde{\boldsymbol{H}}_s\left(\boldsymbol{y},\boldsymbol{y}_n;k\right)^\top + o(1)\right]$$

in the Fraunhofer regime. The remainder $o(1)$ is given explicitly with respect to the Fraunhofer parameters by: $\mathcal{O}\left(a^4\Theta_a/L^4\right) + \mathcal{O}(a^2\Theta_b/L^2) + \mathcal{O}\left(a^3/L^3\right)$.

Proof. The proof is an immediate consequence of the definition of the imaging function (14) and the asymptotic formulas (40) and (45).   □

5.4. **Cross-range estimates of position and polarizability tensor.** To study the cross-range resolution of the Kirchhoff image we consider, without loss of generality, the case of a single dipole located at $\boldsymbol{y}_* = (\boldsymbol{y}_{*,\parallel}, L + \eta_*)$ with associated polarizability tensor $\boldsymbol{\alpha}_*$. The following proposition characterizes the decay of the Kirchhoff image in the cross-range away from the dipole position.

Proposition 2 (Imaging function decrease in cross-range)**.** *The Kirchhoff imaging function (14) of a dipole located at $\boldsymbol{y}_* = (\boldsymbol{y}_{*,\parallel}, L + \eta_*)$ and evaluated at $\boldsymbol{y} = (\boldsymbol{y}_\parallel, L + \eta_*)$ satisfies*

- *If the imaging point does not coincide with the dipole in cross-range, ie $\boldsymbol{y}_\parallel \neq \boldsymbol{y}_{*,\parallel}$ then*

(47)
$$\|\mathcal{I}_{KM}(\boldsymbol{y};k)\| = \frac{1}{(4\pi L)^2}\left[\frac{a^2}{L^2}\left(\mathcal{O}\Big(\frac{L}{a\,k|\boldsymbol{y}_\parallel - \boldsymbol{y}_{*,\parallel}|}\Big) + o(1)\right)\right],$$

  for any matrix norm and where $o(1)$ is explicitly given by $\mathcal{O}\left(a^2\Theta_a/L^2\right) + \mathcal{O}(\Theta_b) + \mathcal{O}\left(a/L\right)$.
- *If the imaging point coincides with the dipole in cross-range, i.e. $\boldsymbol{y}_\parallel = \boldsymbol{y}_{*,\parallel}$ then*

(48)
$$\mathcal{I}_{KM}(\boldsymbol{y}_*;k) = \frac{1}{(4\pi L)^2}\left[\frac{\operatorname{mes}\mathcal{A}}{(4\pi L)^2}\boldsymbol{P}_\parallel\,\boldsymbol{\alpha}_*\,\boldsymbol{P}_s + o\Big(\frac{a^2}{L^2}\Big)\right],$$

  where $\operatorname{mes}\mathcal{A} = \Theta(a^2)$ is the area of the array $\mathcal{A}$.[4]

Concretely, proposition 2 shows that the image vanishes asymptotically (compared to its value at $\boldsymbol{y}_*$) provided $|\boldsymbol{y}_\parallel - \boldsymbol{y}_{*,\parallel}|$ is large with respect to the Rayleigh number $L/(ak)$. Hence the characteristic size of the focal spot in the cross-range of a dipole is given by the Rayleigh resolution $L/(ak)$, as is the case in acoustics (see e.g. [11, 14]) or in electromagnetics with collocated sources and receivers [18]. The proof of this proposition is based on the following lemma which approximates the matrix $\widetilde{\boldsymbol{H}}_r\left(\boldsymbol{y},\boldsymbol{y}';k\right)$ in Fraunhofer regime.

Lemma 1. *For $\boldsymbol{y} = (\boldsymbol{y}_\parallel, L + \eta)$, $\boldsymbol{y}' = (\boldsymbol{y}'_\parallel, L + \eta')$ with $\boldsymbol{y}_\parallel \neq \boldsymbol{y}'_\parallel$, the matrix $\widetilde{\boldsymbol{H}}_r(\boldsymbol{y},\boldsymbol{y}';k)$ defined by (41) has the asymptotic expansion*

(49)
$$\|\widetilde{\boldsymbol{H}}_r(\boldsymbol{y},\boldsymbol{y}';k)\| = \frac{a^2}{L^2}\mathcal{O}\Big(\frac{L}{a\,k|\boldsymbol{y}_\parallel - \boldsymbol{y}'_\parallel|}\Big),$$

---

[4]The notation $f(x) = \Theta(g(x))$ means that there are constants $c, C > 0$ such that $cg(x) \le f(x) \le Cg(x)$ in an appropriate limit for x.

in the Fraunhofer regime and for any matrix norm. The constant in the $\mathcal{O}$ notation depends only on the shape of the array $\mathcal{A}$. For $\boldsymbol{y}' = \boldsymbol{y}$, one has

$$(50) \qquad \widetilde{\boldsymbol{H}}_r(\boldsymbol{y}, \boldsymbol{y}; k) = \frac{\mathrm{mes}\,\mathcal{A}}{(4\pi L)^2} \boldsymbol{P}_\parallel,$$

where $\mathrm{mes}\,\mathcal{A} = \Theta(a^2)$ *is the array area.*

Lemma 1 is proved in appendix C.

Proof of proposition 2. The formulas (47) and (48) are a straightforward consequence of proposition 1, lemma 1 and the fact that $\widetilde{\boldsymbol{H}}_s(\boldsymbol{y}_*, \boldsymbol{y}_*; k) = \boldsymbol{P}_s$. $\qquad\square$

Remark 4. *In the particular case where the receiver array $\mathcal{A}$ is a square of side a, one has $\mathrm{mes}\,\mathcal{A} = a^2$ and by evaluating the Fourier transform of the indicator function $\mathbb{1}_\mathcal{A}$, one finds the following explicit expression of the matrix $\widetilde{\boldsymbol{H}}_r(\boldsymbol{y}, \boldsymbol{y}'; k)$:*

$$(51) \quad \widetilde{\boldsymbol{H}}_r(\boldsymbol{y}, \boldsymbol{y}'; k) = a^2 \frac{\exp[\imath k(\eta' - \eta)]}{(4\pi L)^2} \,\mathrm{sinc}\left(\frac{k\,a(y_1 - y_1')}{2\,L}\right) \mathrm{sinc}\left(\frac{k\,a(y_2 - y_2')}{2L}\right) \boldsymbol{P}_\parallel,$$

with $\boldsymbol{y}_\parallel = (y_1, y_2)$ *and* $\boldsymbol{y}_\parallel' = (y_1', y_2')$.

We now consider the problem of recovering the polarizability tensors $\boldsymbol{\alpha}_i$ of the N dipoles. As in [18], the idea is to observe that at each dipole position $\boldsymbol{y}_i$ we have

$$(52)$$
$$\boldsymbol{H}_r(\boldsymbol{y}_i, \boldsymbol{y}_i; k)\,\boldsymbol{\alpha}_i\,\boldsymbol{H}_s(\boldsymbol{y}_i, \boldsymbol{y}_i; k) = \mathcal{I}_{KM}(\boldsymbol{y}_i; k) - \sum_{j \neq i} \boldsymbol{H}_r(\boldsymbol{y}_i, \boldsymbol{y}_j; k)\,\boldsymbol{\alpha}_j\,\boldsymbol{H}_s(\boldsymbol{y}_i, \boldsymbol{y}_j; k)^\top.$$

If the dipoles are well-separated, lemma 1 guarantees that the terms in (52) involving the dipoles $j \neq i$ remain small. Thus, we expect a good estimate of the polarizability tensor $\boldsymbol{\alpha}_i$ by solving the linear system

$$(53) \qquad \widetilde{\boldsymbol{H}}_r(\boldsymbol{y}, \boldsymbol{y}; k)\,\boldsymbol{\alpha}\,\widetilde{\boldsymbol{H}}_s(\boldsymbol{y}, \boldsymbol{y}; k) = \mathcal{I}_{KM}(\boldsymbol{y}; k),$$

for each point $\boldsymbol{y}$ of the imaging window. Notice that we replaced the matrices $\boldsymbol{H}_r$ and $\boldsymbol{H}_s$ by their Fraunhofer regime approximations $\widetilde{\boldsymbol{H}}_r(\boldsymbol{y}, \boldsymbol{y}; k)$ and $\widetilde{\boldsymbol{H}}_s(\boldsymbol{y}, \boldsymbol{y}; k)$. Up to scaling factors, these latter matrices are close to the rank two projectors $\boldsymbol{P}_\parallel$ and $\boldsymbol{P}_s$, respectively. Therefore we cannot expect to retrieve the full polarizability tensor $\boldsymbol{\alpha}$ in the Fraunhofer regime. At most, we expect to recover only the tensor $\boldsymbol{\alpha}$ projected on the range of $\boldsymbol{P}_\parallel$ (on the left) and the range of $\boldsymbol{P}_s$ (on the right), that is the 2×2 matrix $\widetilde{\boldsymbol{\alpha}} = \boldsymbol{U}_\parallel^* \boldsymbol{\alpha}\, \boldsymbol{U}_s$. Indeed, using (46) for $\boldsymbol{y}' = \boldsymbol{y}$, (50) and (37), we rewrite (53) as:

$$(54) \qquad \frac{\mathrm{mes}\,\mathcal{A}}{(4\pi L)^2} \boldsymbol{U}_\parallel \boldsymbol{U}_\parallel^* \boldsymbol{\alpha} \frac{1}{(4\pi L)^2} \boldsymbol{U}_s \boldsymbol{U}_s^* = \mathcal{I}_{KM}(\boldsymbol{y}; k).$$

Multiplying on the left by $(L^2/\mathrm{mes}\,\mathcal{A})\,\boldsymbol{U}_\parallel^*$ and on the right by $(4\pi L)^2 \boldsymbol{U}_s$ gives

$$(55) \qquad \widetilde{\boldsymbol{\alpha}} = \frac{(4\pi L)^4}{\mathrm{mes}\,\mathcal{A}} \widetilde{\mathcal{I}}_{KM}(\boldsymbol{y}; k),$$

where $\widetilde{\mathcal{I}}_{KM}(\boldsymbol{y}; k)$ is also defined by $\widetilde{\mathcal{I}}_{KM}(\boldsymbol{y}; k) = \boldsymbol{U}_\parallel^* \mathcal{I}_{KM}(\boldsymbol{y}; k)\,\boldsymbol{U}_s$. In the following theorem, the Frobenius matrix norm is denoted by $\|\cdot\|_F$.

Theorem 2. *(Cross-range estimation of the polarizability tensor) Let $\widetilde{\boldsymbol{\alpha}}$ and $\widetilde{\boldsymbol{\alpha}}_i$ be the 2×2 matrices defined by $\widetilde{\boldsymbol{\alpha}} = \boldsymbol{U}_\parallel^* \boldsymbol{\alpha}\, \boldsymbol{U}_s$ and $\boldsymbol{\alpha}_i = \boldsymbol{U}_\parallel^* \boldsymbol{\alpha}_i \boldsymbol{U}_s$. Then we have the following*

- *If the imaging point coincides with the dipole, i.e. $\boldsymbol{y} = \boldsymbol{y}_i$,*

$$(56) \quad \|\widetilde{\boldsymbol{\alpha}} - \widetilde{\boldsymbol{\alpha}}_i\|_F = \mathcal{O}\Big(\frac{L}{a\,k\,\min\limits_{j \neq i}|\boldsymbol{y}_{i,\|} - \boldsymbol{y}_{j,\|}|}\Big) + \mathcal{O}\Big(\frac{a}{L}\Big) + \mathcal{O}\Big(\frac{a^2\Theta_a}{L^2}\Big) + \mathcal{O}\left(\Theta_b\right).$$

- *If the imaging point does not coincide with a dipole in cross-range, i.e. if $\boldsymbol{y} \neq \boldsymbol{y}_j$ for all $j = 1, \ldots, N$,*

$$(57) \quad \|\widetilde{\boldsymbol{\alpha}}\|_F = \mathcal{O}\Big(\frac{L}{a\,k\,\min\limits_{j=1,\ldots,N}|\boldsymbol{y}_\| - \boldsymbol{y}_{j,\|}|}\Big) + \mathcal{O}\Big(\frac{a^2\Theta_a}{L^2}\Big) + \mathcal{O}\left(\Theta_b\right).$$

Proof. We first prove the asymptotic relation (56) when $\boldsymbol{y} = \boldsymbol{y}_i$. One checks easily by first left and right multiplying both sides of (52) respectively by $((4\pi L)^2/\operatorname{mes}\mathcal{A})\,\boldsymbol{U}_\|^*$ and $(4\pi L)^2\boldsymbol{U}_s$ and then using the asymptotic formula (40) and (45) that

$$\widetilde{\boldsymbol{\alpha}}_i = \frac{(4\pi L)^4}{\operatorname{mes}\mathcal{A}}\Big[\widetilde{\mathcal{I}}(\boldsymbol{y}_i; k) - \sum_{j \neq i}\boldsymbol{U}_\|^*\boldsymbol{H}_r\left(\boldsymbol{y}_i, \boldsymbol{y}_j; k\right)\,\boldsymbol{\alpha}_j\,\boldsymbol{H}_s\left(\boldsymbol{y}_i, \boldsymbol{y}_j; k\right)^\top\boldsymbol{U}_s + \frac{1}{L^2}o\Big(\frac{a^2}{L^2}\Big)\Big],$$

where $o(a^2/L^2)$ is explicitly given by $\mathcal{O}(a^4\Theta_a/L^4) + \mathcal{O}(a^2\Theta_b/L^2) + \mathcal{O}(a^3/L^3)$. Thus it follows immediately from (55) that

$$(58) \quad \widetilde{\boldsymbol{\alpha}} - \widetilde{\boldsymbol{\alpha}}_i = \frac{(4\pi L)^4}{\operatorname{mes}\mathcal{A}}\Big[\sum_{j \neq i}\boldsymbol{U}_\|^*\boldsymbol{H}_r\left(\boldsymbol{y}_i, \boldsymbol{y}_j; k\right)\,\boldsymbol{\alpha}_j\,\boldsymbol{H}_s\left(\boldsymbol{y}_i, \boldsymbol{y}_j; k\right)^\top\boldsymbol{U}_s + \frac{1}{L^2}o\Big(\frac{a^2}{L^2}\Big)\Big],$$

where $o(a^2/L^2) = \mathcal{O}(a^4\Theta_a/L^4) + \mathcal{O}(a^2\Theta_b/L^2) + \mathcal{O}(a^3/L^3)$.
Finally we conclude by using that $\operatorname{mes}\mathcal{A} = \Theta(a^2)$, $\|\boldsymbol{U}_\|^*\|_F = \|\boldsymbol{U}_s\|_F = \sqrt{2}$, and the asymptotic expansion (47) to control the coupling terms

$$\|\sum_{j \neq i}\boldsymbol{H}_r\left(\boldsymbol{y}_i, \boldsymbol{y}_j; k\right)\,\boldsymbol{\alpha}_j\,\boldsymbol{H}_s\left(\boldsymbol{y}_i, \boldsymbol{y}_j; k\right)^\top\|_F.$$

The asymptotic expansion (57) where $\boldsymbol{y} \neq \boldsymbol{y}_i$ is an immediate consequence of the reconstruction formula (55), $\operatorname{mes}\mathcal{A} = \Theta(a^2)$, proposition 2 which expresses the decay of the Kirchhoff image $\|\mathcal{I}_{KM}(\boldsymbol{y}; k)\|_F$ in the case of one dipole and the linearity of $\mathcal{I}_{KM}(\boldsymbol{y}; k)$ with respect to the data. $\qquad\square$

Theorem 2 and estimate (56) guarantee a good estimate of $\widetilde{\boldsymbol{\alpha}}_i$ using the reconstruction formula (55) at the dipole position $\boldsymbol{y}_i$, provided the cross-range distance to the closest dipole is large compared to the Rayleigh criterion $L/(ka)$. The other error terms vanish in the Fraunhofer asymptotic regime. The second estimate (57) shows that $\|\widetilde{\boldsymbol{\alpha}}\|_F$ at an imaging point $\boldsymbol{y}$ decays as the inverse of the cross-range distance to the closest dipole. Thus, $\|\widetilde{\boldsymbol{\alpha}}\|_F$ is also a good imaging function for the cross-range position of the dipoles. Indeed, it has the same cross-range resolution $L/(ak)$ (see (57)) as the Kirchhoff imaging function $\mathcal{I}_{KM}(\boldsymbol{y}; k)$ (see proposition 2).

5.5. **Estimates of range position and polarizability tensor.** We now assume that the data (7) is available over a frequency band $[\omega_0 - B/2, \omega_0 + B/2]$ of central (angular) frequency ω_0 and bandwidth B. The Kirchhoff image of the multi-frequency data is given by integrating over the frequency band the single frequency Kirchhoff imaging function (14), that is

$$(59) \quad \mathcal{I}_{KM}(\boldsymbol{y}) = \int_{|\omega-\omega_0|<B/2} d\omega\,\mathcal{I}_{KM}\left(\boldsymbol{y}; \frac{\omega}{c}\right).$$

We further assume that the dipoles are standard scatterers, i.e. their rescaled polarizability tensor $\boldsymbol{\alpha}(\boldsymbol{y}, \omega) = \mu \omega^2 \boldsymbol{\alpha}'(\boldsymbol{y}, \omega)$ is constant with respect to the frequency on the frequency bandwidth B. This a usually a good approximation for dielectrics or metals at high frequency (see e.g. [43]) where the "physical" polarizability tensor is shown to be $\boldsymbol{\alpha}'(\boldsymbol{y}, \omega) = \mathcal{O}(\omega^{-2})$ as $\omega \to \infty$.

We now estimate the range resolution of the imaging function (59). Without loss of generality, we consider the case of a single dipole $\boldsymbol{y}_* = (\boldsymbol{y}_{*,\|}, L + \eta_*)$ whose cross-range position $\boldsymbol{y}_{*,\|}$ is known. For the analysis and in the following, we assume that all the asymptotic expansions of section 5.1 hold uniformly with $k = \omega/c$ in the frequency band.

Let $\boldsymbol{y} = (\boldsymbol{y}_{*,\|}, L + \eta)$ be an imaging point. With proposition 1 we see that the imaging function (59) satisfies

$$\mathcal{I}_{KM}(\boldsymbol{y}) = \frac{1}{(4\pi L)^2} \int_{|\omega - \omega_0| < B/2} d\omega \, \widetilde{\boldsymbol{H}}_r\Big(\boldsymbol{y}, \boldsymbol{y}_*; \frac{\omega}{c}\Big) \boldsymbol{\alpha}_* \widetilde{\boldsymbol{H}}_s\Big(\boldsymbol{y}, \boldsymbol{y}_*; \frac{\omega}{c}\Big)^\top + \frac{B}{(4\pi L)^2} o\Big(\frac{a^2}{L^2}\Big),$$

where the $o(a^2/L^2)$ term can be explicitly given by $\mathcal{O}\left(a^4 \Theta_a/L^4\right) + \mathcal{O}(a^2 \Theta_b/L^2) + \mathcal{O}\left(a^3/L^3\right)$ (see proposition 1). Hence we get that
(60)
$$\mathcal{I}_{KM}(\boldsymbol{y}) = \frac{\operatorname{mes}\mathcal{A}}{(4\pi L)^4} \boldsymbol{P}_\| \boldsymbol{\alpha}_* \boldsymbol{P}_s \int_{|\omega - \omega_0| < B/2} d\omega \, \exp[\imath\omega \left(\phi(\eta_*) - \phi(\eta)\right)/c] + \frac{B}{(4\pi L)^2} o\Big(\frac{a^2}{L^2}\Big),$$

where ϕ is the smooth phase function

$$\phi(\eta) = \eta + |\boldsymbol{x}_s - \boldsymbol{y}| = \eta + \sqrt{|\boldsymbol{y}_\| - \boldsymbol{x}_{s,\|}|^2 + (L + \eta - x_{s,3})^2}.$$

The integral over the frequency band can then be evaluated explicitly to obtain
(61)
$$\mathcal{I}_{KM}(\boldsymbol{y}) = \frac{B \operatorname{mes}\mathcal{A}}{(4\pi L)^4} \boldsymbol{P}_\| \boldsymbol{\alpha}_* \boldsymbol{P}_s \exp[\imath\omega_0\left(\phi(\eta_*) - \phi(\eta)\right)/c] \operatorname{sinc}\Big(\frac{B\left(\phi(\eta_*) - \phi(\eta)\right)}{2\,c}\Big)$$
$$+ \frac{B}{(4\pi L)^2} o\left(\frac{a^2}{L^2}\right).$$

The next proposition shows that as soon as the range distance $|\eta - \eta_*|$ between the imaging point and the dipole becomes large compared to c/B, the norm of the Kirchhoff imaging function (62) becomes small compared to its value at the dipole position (63). Thus the range resolution is given by c/B (as in acoustics [11, 14] or in electromagnetics with collocated sources and receivers [18]).

Proposition 3 (Range resolution of the position). *Assume the geometric condition* (20) *holds for the source. The Kirchhoff imaging function* (59) *of a dipole located at* $\boldsymbol{y}_* = (\boldsymbol{y}_{*,\|}, L + \eta_*)$ *and evaluated at* $\boldsymbol{y} = (\boldsymbol{y}_{*,\|}, L + \eta)$ *satisfies*

(62) $\qquad \|\mathcal{I}_{KM}(\boldsymbol{y}; k)\| = \dfrac{B}{(4\pi L)^2} \dfrac{a^2}{L^2} \left(\mathcal{O}\Big(\dfrac{c}{B\,|\eta - \eta_*|}\Big) + o(1)\right), \quad \text{when } \eta \neq \eta_*,$

for any matrix norm. The remainder $o(1)$ *term can be explicitly given by* $\mathcal{O}\left(a^2 \Theta_a/L^2\right) + \mathcal{O}(\Theta_b) + \mathcal{O}\left(b/L\right)$. *When* $\eta = \eta_*$, *one has*

(63) $\qquad \mathcal{I}_{KM}(\boldsymbol{y}_*; k) = \dfrac{B}{(4\pi L)^2} \left[\dfrac{\operatorname{mes}\mathcal{A}}{(4\pi L)^2} \boldsymbol{P}_\| \boldsymbol{\alpha}_* \boldsymbol{P}_s + o\Big(\dfrac{a^2}{L^2}\Big)\right],$

where $\operatorname{mes}\mathcal{A} = \Theta(a^2)$ *is the area of the array.*

Proof. Since ϕ is a smooth function, the mean value theorem implies that

$$(64) \qquad |(\phi(\eta) - \phi(\eta_*))^{-1}| \leq \max_{\boldsymbol{y}' \in \mathcal{W}} |\phi'(\eta')^{-1}| \, |\eta - \eta_*|^{-1} = \mathcal{O}(|\eta - \eta_*|^{-1}),$$

where $\boldsymbol{y}' = (\boldsymbol{y}'_\|, L + \eta')$ is a point belonging to the imaging window $\mathcal{W}$. In (64) we can use $\phi'(\eta')^{-1}$ because

$$(65) \qquad \phi'(\eta') = 1 + \frac{L + \eta' - x_{s,3}}{|\boldsymbol{x}_s - \boldsymbol{y}'|} \neq 0$$

since $\boldsymbol{y}'_\| \neq \boldsymbol{x}_{s,\|}$. This last condition on the cross-range of the source is weaker than the geometric condition imposed in (20) since the characteristic size b of the imaging widow is small compared to characteristic size a of the array of receivers. As $\mathcal{W}$ is a compact set, this implies that $\max_{\boldsymbol{y}' \in \mathcal{W}} |(\phi'(\eta'))^{-1}|$ exists in (64). Thus, it follows form (64) that

$$(66) \qquad \mathrm{sinc}\left(\frac{B(\phi(\eta_*) - \phi(\eta))}{2\,c}\right) = \mathcal{O}\left(\frac{c}{B\,|\eta - \eta_*|}\right).$$

Thus, the asymptotic expansion(62) is an immediate consequence of (61), (66) and the fact that $\mathrm{mes}\,\mathcal{A} = \mathcal{O}(a^2)$. Finally, the asymptotic relation (63) follows immediately by evaluating (60) at $\boldsymbol{y} = \boldsymbol{y}_*$. $\qquad\square$

Since we assume the polarizability tensor $\boldsymbol{\alpha}$ is frequency independent (see section 2), we suggest to estimate it by averaging the single frequency estimate (56) over the frequency band

$$(67) \qquad \widetilde{\boldsymbol{\alpha}} = \frac{1}{B} \int_{\mathcal{B}} d\omega \, \widetilde{\boldsymbol{\alpha}}(\omega).$$

Note that (67) involves the projected polarizability tensor $\widetilde{\boldsymbol{\alpha}} = \boldsymbol{U}_\|^* \boldsymbol{\alpha} \boldsymbol{U}_s$ (which is estimated in (55) from the Kirchhoff image), and the matrices $\boldsymbol{U}_\|^*$ and $\boldsymbol{U}_s$ are frequency independent. Hence it is straightforward to check that integrating the single frequency estimate (56) and (57) with (67) over the frequency band does not change these cross-range resolution estimates.

Here we study the effect of the other dipoles in the polarizability tensor estimate in range. We isolate the effect of range by considering the case where all the dipoles have same cross-range, i.e. $\boldsymbol{y}_i = (\boldsymbol{y}_{*,\|}, L + \eta_i)$ for $i = 1, \ldots, N$. The following proposition shows that the depth resolution of the reconstructed $\widetilde{\boldsymbol{\alpha}}$ is also c/B. Concretely, the estimate (68) shows that one has a good depth resolution of $\widetilde{\boldsymbol{\alpha}}_i$ by the reconstruction formula (67) at the dipole position $\boldsymbol{y}_i$, as soon as the range distance of the different dipoles is large compared to c/B. The second estimate (69) shows that $\|\widetilde{\boldsymbol{\alpha}}\|_F$ at an imaging point $\boldsymbol{y}$ decays when the range distance to the closest dipole becomes large compared to c/B. Thus, $\|\widetilde{\boldsymbol{\alpha}}\|_F$ is also a good imaging function for the range position of a dipole with the same depth resolution c/B (see (69)) as the Kirchhoff imaging function (see proposition 3).

Theorem 3. *Assume the geometric condition* (20) *holds for the source and the dipoles are all aligned in the range direction of* $\mathcal{A}$. *The image of the cross-range polarizability tensor* $\widetilde{\boldsymbol{\alpha}}$ *(given by* (67)*) satisfies the two following estimates:*

- *If the imaging point is the dipole location, i.e.* $\boldsymbol{y} = \boldsymbol{y}_i$, *we have*

$$(68) \qquad \|\widetilde{\boldsymbol{\alpha}} - \widetilde{\boldsymbol{\alpha}}_i\|_F = \mathcal{O}\left(\frac{c}{B \min_{j \neq i} |\eta_i - \eta_j|}\right) + o(1),$$

- *If the imaging point range is different from any of the dipole ranges,* $\boldsymbol{y} = (\boldsymbol{y}_{*,\parallel}, L + \eta) \neq \boldsymbol{y}_j$, *for all* $j = 1, \ldots, N$,

(69) $$\|\widetilde{\boldsymbol{\alpha}}\|_F = \mathcal{O}\Big(\frac{c}{B \min\limits_{j=1,\ldots,N} |\eta - \eta_j|} \Big) + o(1).$$

Proof. We first show the asymptotic expansion (68), i.e. when $\boldsymbol{y} = \boldsymbol{y}_i$. Since $\boldsymbol{\alpha}_i$, $\boldsymbol{U}_\parallel$ and $\boldsymbol{U}_s$ are frequency independent, one has

(70) $$\widetilde{\boldsymbol{\alpha}} - \widetilde{\boldsymbol{\alpha}}_i = \frac{1}{B} \int_B d\omega \, (\widetilde{\boldsymbol{\alpha}}(\omega) - \widetilde{\boldsymbol{\alpha}}_i).$$

Hence (58) and the previous expression gives that

$$\widetilde{\boldsymbol{\alpha}} - \widetilde{\boldsymbol{\alpha}}_i = \frac{(4\pi L)^4}{B \operatorname{mes} \mathcal{A}} \int_B \Big[\boldsymbol{U}_\parallel^* \big(\sum_{j \neq i} \boldsymbol{H}_r\left(\boldsymbol{y}_i, \boldsymbol{y}_j; k\right) \boldsymbol{\alpha}_j \, \boldsymbol{H}_s\left(\boldsymbol{y}_i, \boldsymbol{y}_j; k\right)^\top \big) \boldsymbol{U}_s + o\Big(\frac{a^2}{L^2} \Big) \Big].$$

Now recall $(\operatorname{mes} \mathcal{A})^{-1} = \mathcal{O}(a^{-2})$. Using the expression (61) of the imaging function for aligned dipoles we get

$$\widetilde{\boldsymbol{\alpha}} - \widetilde{\boldsymbol{\alpha}}_i = \sum_{j \neq i} \widetilde{\boldsymbol{\alpha}}_j \exp[\imath\omega_0\big(\phi(\eta_j) - \phi(\eta_i)\big)/c] \operatorname{sinc}\Big(\frac{B\big(\phi(\eta_j) - \phi(\eta_i)\big)}{2\,c} \Big) + o(1).$$

We arrive to (68) by using the asymptotic relation (64) (which holds under the geometric condition) to control the sinc and the fact that $\widetilde{\boldsymbol{\alpha}}_j = \mathcal{O}(1)$. Finally, the asymptotic formula (69) can be proved from the relation (67) in a similar way. $\square$

5.6. **Correction of oscillatory artifacts.** In acoustics, it is a well-known that the reflection coefficient of a point scatterer can only be recovered up to a complex phase, see e.g. [42]. A similar phenomenon is observed in electromagnetism. For the case of collocated sources and receivers [18], the polarizability tensor of a dipole is for all practical purposes, recovered only up to a complex phase because the Kirchhoff imaging function oscillates in range. These oscillatory artifacts can be corrected by fixing the phase of one of the components of the estimated polarizability tensor [18]. In the non-collocated sources and receivers case, we observe oscillatory artifacts in range (fig. 8) and also in cross-range (fig. 7). Here we explain where these oscillatory artifacts come from and why they also occur in cross-range. Both oscillatory artifacts can be corrected in the same manner as in [18], as is illustrated in figs. 7 and 8.

To observe the oscillations in the range direction, we consider the reconstruction formula (67) in the case of a single dipole ($N = 1$) located at $\boldsymbol{y}_*$ with polarizability tensor $\boldsymbol{\alpha}_*$, and for imaging points of the form $\boldsymbol{y} = (\boldsymbol{y}_{*,\parallel}, L + \eta)$. Using (55), proposition 1 with the relations (41), (46) and integrating over the bandwidth, we rewrite (67) as

$$\begin{aligned} \widetilde{\boldsymbol{\alpha}} &= \int_{|\omega - \omega_0| < B/2} d\omega \, \exp\Big[\imath\frac{\omega}{c} \left(\phi(\eta_*) - \phi(\eta)\right) \Big] \widetilde{\boldsymbol{\alpha}}_* + o(1) \\ &= \exp\Big[\imath\frac{\omega_0}{c}(\phi(\eta_*) - \phi(\eta)) \Big] \operatorname{sinc}\Big(\frac{B(\phi(\eta_*) - \phi(\eta))}{c} \Big) \widetilde{\boldsymbol{\alpha}}_* + o(1). \end{aligned}$$

Under the geometric condition (20), we have $\phi(\eta_*) - \phi(\eta) = \phi'(\eta_*)(\eta_* - \eta) + o(\eta - \eta_*)$ with $0 < \phi'(\eta_*) < 2$ (see (65)), thus the presence of the complex exponential $\exp[\imath\omega_0\left(\phi(\eta_*) - \phi(\eta)/c\right)]$ and the sinc causes the image of $\widetilde{\boldsymbol{\alpha}}$ to oscillate in η around the dipole range position η_*. Compared to the case of collocated sources and

receivers [18], where the function ϕ is replaced by η, the presence of the factor $\phi'(\eta_*)$ in the Taylor expansion of ϕ around η_* takes into account the relative positions of the source, the array and the dipole. Furthermore, if the source range $x_{s,3}$ is between the array and the imaging points, i.e. if $0 < x_{s,3} < L + \eta$ for all imaging points, one has by (65) that $1 < \phi'(\eta_*) < 2$. Thus, if the central angular frequency ω_0 and the bandwidth B are of the same order, *the oscillations' length-scale is c/B, the focal spot size in depth.* Therefore, if the range position $L + \eta_*$ of the dipole is not known precisely, we cannot expect to accurately reconstruct $\widetilde{\alpha}_*$.

We deal with this artifact by fixing the phase of one component of the 2×2 matrix $\widetilde{\alpha}$, as in [18]. The choice we made here is to enforce that the $1, 1$ entry be real and positive, i.e. $\arg(\widetilde{\alpha}_{1,1}) = 0$. This can be achieved by post-processing the reconstruction formula (67) by the operation $(\overline{\widetilde{\alpha}_{1,1}}/|\widetilde{\alpha}_{1,1}|)\,\widetilde{\alpha}$. If the coefficient $|\widetilde{\alpha}_{1,1}|$ is small, this operation can be problematic. If necessary, the phase of another coefficient of $\widetilde{\alpha}$ can be fixed or we can regularize by using $(\overline{\widetilde{\alpha}_{1,1}}/(|\widetilde{\alpha}_{1,1}| + \delta))\widetilde{\alpha}$, for a small $\delta > 0$.

To explain the oscillations in the cross-range direction, we evaluate the single frequency reconstruction formula (55) using proposition 1, (41) and (46) at image points $\boldsymbol{y} = (\boldsymbol{y}_\parallel, L + \eta_*)$ in the cross-range of the dipole $\boldsymbol{y}_*$ to get

$$(71) \qquad \widetilde{\boldsymbol{\alpha}} = \exp\left[\imath k[\psi(\boldsymbol{y}_{*,\parallel}) - \psi(\boldsymbol{y}_\parallel)]\right] \mathcal{F}[\mathbb{1}_{\mathcal{A}}]\left(\frac{k}{L}(\boldsymbol{y}_{*,\parallel} - \boldsymbol{y}_\parallel)\right)\widetilde{\boldsymbol{\alpha}}_* + o(1),$$

where the $o(1)$ remainder can be given explicitly by $\mathcal{O}\left(a^2\Theta_a/L^2\right) + \mathcal{O}(\Theta_b) + \mathcal{O}\left(a/L\right)$ and the smooth function ψ is defined by $\psi(\boldsymbol{y}_\parallel) = |\boldsymbol{x}_s - \boldsymbol{y}|$. To give an explicit expression of these oscillations, we assume that $\mathcal{A}$ is a square of side a. Hence (71) can be computed explicitly with the Fourier transform of $\mathbb{1}_{\mathcal{A}}$ (as in (51)):

$$\widetilde{\boldsymbol{\alpha}} = \exp\left[\imath k[\psi(\boldsymbol{y}_{*,\parallel}) - \psi(\boldsymbol{y}_\parallel)]\right] \operatorname{sinc}\left(\frac{k\,a(\boldsymbol{y}_{*,1} - \boldsymbol{y}_1)}{2L}\right) \operatorname{sinc}\left(\frac{k\,a(\boldsymbol{y}_{*,2} - \boldsymbol{y}_2)}{2L}\right)\widetilde{\boldsymbol{\alpha}}_* + o(1).$$

In the last formula, we have

$$\psi(\boldsymbol{y}_{*,\parallel}) - \psi(\boldsymbol{y}_\parallel) = \nabla\psi_{\boldsymbol{y}_{*,\parallel}} \cdot (\boldsymbol{y}_{*,\parallel} - \boldsymbol{y}_\parallel) + o(|\boldsymbol{y}_{*,\parallel} - \boldsymbol{y}_\parallel|) \text{ with } \nabla\psi_{\boldsymbol{y}_{*,\parallel}} = \frac{\boldsymbol{x}_{s,\parallel} - \boldsymbol{y}_{*,\parallel}}{|\boldsymbol{x}_s - \boldsymbol{y}_*|}.$$

Notice that $\nabla\psi_{\boldsymbol{y}_{*,\parallel}} \neq 0$ since $\boldsymbol{x}_{s,\parallel} \neq \boldsymbol{y}_{*,\parallel}$ under the geometrical condition (20). On one hand, the presence of the sinc terms induces an oscillation whose length scale is given by the Rayleigh criterion ka/L, the cross-range focal spot size. On the other hand, the complex exponential $\exp\left[\imath k[\psi(\boldsymbol{y}_{*,\parallel}) - \psi(\boldsymbol{y}_\parallel)]\right]$ induces an oscillation whose length scale is controlled in each cross-range direction (at the vicinity of $\boldsymbol{y}_*$) by $2\pi/(k|\nabla\psi_{\boldsymbol{y}_{*,\parallel}}|)$ and thus could rapidly change with $|\boldsymbol{x}_s - \boldsymbol{y}_*|$. With these oscillations, one cannot expect to reconstruct $\widetilde{\boldsymbol{\alpha}}$ accurately in cross-range. Of course, the same post-processing operation $(\overline{\alpha_{1,1}}/|\widetilde{\alpha}_{1,1}|)\,\widetilde{\boldsymbol{\alpha}}$ eliminates the oscillation artifacts in both range and cross-range images of $\widetilde{\boldsymbol{\alpha}}$. This is illustrated by the numerical experiments in figs. 7 and 8.

5.7. Physical measurements. We now show that the full data $\boldsymbol{\Pi}$ is not necessary to obtain Kirchhoff images. We consider here the case where we only have access to the projected data $\boldsymbol{P}_\parallel\boldsymbol{\Pi}\boldsymbol{P}_s = \boldsymbol{U}_\parallel\widetilde{\boldsymbol{\Pi}}\boldsymbol{U}_s^*$ (where $\widetilde{\boldsymbol{\Pi}}$ defined by (12)). This is a more physically relevant setup as it assumes only the electric field components parallel to the array can be measured and that the source polarization can only be controlled in the two dimensional subspace $(\boldsymbol{x}_s - \boldsymbol{y}_0)^\perp$ (see sections 2.2 and 3.2). To this end, we show that the Kirchhoff imaging functions $\mathcal{I}_{KM}[\boldsymbol{P}_\parallel\boldsymbol{\Pi}\boldsymbol{P}_s]$ and $\mathcal{I}_{KM}[\boldsymbol{\Pi}]$ have the

same cross-range and range resolutions. In other words the additional information contained in the full data problem does not bring any new information about the position, at least in the Fraunhofer regime. This can be expected because the wave emanating from the source is close to a plane wave in the vicinity of the scatterer, making one component of the electric field irrelevant. Similarly the scattered wave is a close to a plane wave near the array (see section 2.2).

Proposition 4. *The imaging function $\mathcal{I}_{KM}[\boldsymbol{P}_\parallel \boldsymbol{\Pi} \boldsymbol{P}_s](\cdot; k)$ satisfies the asymptotic relation* (47) *and the asymptotic relation* (48)*. The multi-frequency imaging function $\mathcal{I}_{KM}[\boldsymbol{P}_\parallel \boldsymbol{\Pi} \boldsymbol{P}_s](\cdot)$ satisfies the asymptotic relations* (62) *and* (63) *in range. Moreover using $\mathcal{I}_{KM}[\boldsymbol{P}_\parallel \boldsymbol{\Pi} \boldsymbol{P}_s](\cdot; k)$ to reconstruct $\widetilde{\boldsymbol{\alpha}}$ over the bandwidth (formulas* (67) *and* (55)*) leads to the same results in range and cross-range. In other words the propositions 2 and 3 hold with the partial data $\boldsymbol{P}_\parallel \boldsymbol{\Pi} \boldsymbol{P}_s$.*

Proof. Using the linearity of the Kirchhoff imaging function with respect to the data, we consider the case of a single dipole located at $\boldsymbol{y}_* = (\boldsymbol{y}_{*,\parallel}, L + \eta_*)$ with polarizability tensor $\boldsymbol{\alpha}_*$. For $\boldsymbol{y} = (\boldsymbol{y}_\parallel, L + \eta_*)$ and partial data $\boldsymbol{P}_\parallel \boldsymbol{\Pi} \boldsymbol{P}_s$ the image is
$$(72)$$
$$\mathcal{I}_{KM}[\boldsymbol{P}_\parallel \boldsymbol{\Pi} \boldsymbol{P}_s](\boldsymbol{y}, k)$$
$$= \int_{\mathcal{A}} d\boldsymbol{x}_{r,\parallel} \, \overline{\boldsymbol{G}(\boldsymbol{x}_r, \boldsymbol{y}; k)} \, \boldsymbol{P}_\parallel \boldsymbol{G}(\boldsymbol{x}_r, \boldsymbol{y}_*; k) \, \boldsymbol{\alpha}(\boldsymbol{y}_*) \boldsymbol{G}(\boldsymbol{y}_*, \boldsymbol{x}_s; k) \, \boldsymbol{P}_s \overline{\boldsymbol{G}(\boldsymbol{x}_s, \boldsymbol{y}; k)}.$$

Using the asymptotic expression of the dyadic Green function (39), we can show in the same way as for the relation (40) that
$$(73)$$
$$\int_{\mathcal{A}} d\boldsymbol{x}_{r,\parallel} \, \overline{\boldsymbol{G}(\boldsymbol{x}_r, \boldsymbol{y}; k)} \, \boldsymbol{P}_\parallel \boldsymbol{G}(\boldsymbol{x}_r, \boldsymbol{y}_*; k) = \widetilde{\boldsymbol{H}}_r(\boldsymbol{y}, \boldsymbol{y}_*; k) + \mathcal{O}\Big(\frac{a^4 \Theta_a}{L^4}\Big) + \mathcal{O}\Big(\frac{a^2 \Theta_b}{L^2}\Big) + \mathcal{O}\Big(\frac{a^3}{L^3}\Big).$$

We now consider the term linked to the source in (72). By applying the asymptotics relation (44), we can show as in (45) that

$$(74) \quad \boldsymbol{G}(\boldsymbol{y}_*, \boldsymbol{x}_s; k) \, \boldsymbol{P}_s \overline{\boldsymbol{G}(\boldsymbol{x}_s, \boldsymbol{y}; k)} = \frac{1}{(4\pi L)^2} \Big[\widetilde{\boldsymbol{H}}_s(\boldsymbol{y}, \boldsymbol{y}_*; k)^\top + O\Big(\frac{b}{L}\Big) + \mathcal{O}\Big(\frac{a^2}{\Theta_a L^2}\Big) \Big].$$

Thus, by combining (73) and (74), we get

$$\mathcal{I}_{KM}[\boldsymbol{P}_\parallel \boldsymbol{\Pi} \boldsymbol{P}_s](\boldsymbol{y}, k) = \frac{1}{(4\pi L)^2} \widetilde{\boldsymbol{H}}_r(\boldsymbol{y}, \boldsymbol{y}_*; k) \, \boldsymbol{\alpha}(\boldsymbol{y}_*) \, \widetilde{\boldsymbol{H}}_s(\boldsymbol{y}, \boldsymbol{y}_*; k)^\top + o(1),$$

where the $o(1)$ remainder can be explicitly given by $\mathcal{O}\left(a^4 \Theta_a / L^4\right) + \mathcal{O}\left(a^2 \Theta_b / L^2\right) + \mathcal{O}\left(a^3 / L^3\right)$. The rest of the proof is identical to the proof of proposition 2 since $\mathcal{I}_{KM}[\boldsymbol{P}_\parallel \boldsymbol{\Pi} \boldsymbol{P}_s](\boldsymbol{y}; k)$ and $\mathcal{I}_{KM}[\boldsymbol{\Pi}](\boldsymbol{y}; k)$ have exactly the same Fraunhofer asymptotic expansion. Thus, the asymptotic expansions (62) and (63) in range can be derived exactly in the same way as in section 5.5. Finally, as these new data have the same asymptotic properties as the full data, doing the same post-processing as in sections 5.4 and 5.5 leads to an accurate reconstruction of $\widetilde{\boldsymbol{\alpha}}$, in both cross-range and range. To be more precise, theorems 2 and 3 can also be proved identically. $\square$

6. The coherency matrix from time domain electric field autocorrelations

Here we show that the coherency matrix data (10) can be obtained from measuring the time domain electric field autocorrelations at the array resulting from

illuminating with a point source that is driven by a random process (i.e. white light). To this end, the assumptions (9) need to be supplemented to account for the frequency dependence of the polarization vector $\boldsymbol{j}_s(\omega)$. Indeed, since the time domain polarization vector $\boldsymbol{j}_s(t)$ is real, $\boldsymbol{j}_s(\omega)$ obeys the reflection principle $\boldsymbol{j}_s(-\omega) = \overline{\boldsymbol{j}_s(\omega)}$. Taking this into account, we must have that for any $\omega, \omega' \in \mathbb{R}$

$$\langle \boldsymbol{j}_s(\omega) \rangle = 0$$

(75) $$\langle \boldsymbol{j}_s(\omega) \boldsymbol{j}_s(\omega')^T \rangle = \delta(\omega + \omega') \boldsymbol{U}_s \widetilde{\boldsymbol{J}}_s(\omega) \boldsymbol{U}_s^*, \text{ and}$$

$$\langle \boldsymbol{j}_s(\omega) \boldsymbol{j}_s(\omega')^* \rangle = \delta(\omega - \omega') \boldsymbol{U}_s \widetilde{\boldsymbol{J}}_s(\omega) \boldsymbol{U}_s^*,$$

where $\widetilde{\boldsymbol{J}}_s(\omega)$ is a (known) 2×2 Hermitian matrix with $\widetilde{\boldsymbol{J}}_s(-\omega) = \overline{\widetilde{\boldsymbol{J}}_s(\omega)}$. With these assumptions it is easy to see that $\boldsymbol{j}_s(t)$ is a real Gaussian stationary random vector satisfying

(76) $$\langle \boldsymbol{j}_s(t) \rangle = \boldsymbol{0}, \text{ and } \langle \boldsymbol{j}_s(t + \tau) \boldsymbol{j}_s(t)^T \rangle = \boldsymbol{U}_s \widetilde{\boldsymbol{J}}_s(\tau) \boldsymbol{U}_s^*,$$

where $\widetilde{\boldsymbol{J}}_s(\tau)$ is the Fourier transform (using the convention (3)) of $\widetilde{\boldsymbol{J}}_s(\omega)$. This is a version of the Wiener-Khinchin theorem (see e.g. [34]) for vectors. The next proposition shows that when using a random source, measuring empirical autocorrelations of the electric field at the array can be used to find the coherency matrix data $\boldsymbol{\psi}(\omega)$ in (10), provided the acquisition time is large.

Proposition 5 (Statistical stability). *Assume $\boldsymbol{j}_s(t)$ is a stationary Gaussian process satisfying (76) and the Born approximation holds. For each $\boldsymbol{x}_r \in \mathcal{A}$, the empirical autocorrelations are*

(77) $$\boldsymbol{\psi}_{emp}(\boldsymbol{x}_r, \tau) = \frac{1}{2T} \int_{-T}^{T} dt \boldsymbol{U}_{\parallel}^* \boldsymbol{E}(\boldsymbol{x}_r, t + \tau) \boldsymbol{E}(\boldsymbol{x}_r, t)^T \boldsymbol{U}_{\parallel}.$$

Their mean is independent of the measurement time T and is given by

(78) $$\langle \boldsymbol{\psi}_{emp}(\boldsymbol{x}_r, \tau) \rangle = (2\pi) \int d\omega e^{-\imath \omega \tau} \boldsymbol{\psi}(\boldsymbol{x}_r, \omega),$$

Moreover, the empirical autocorrelations are ergodic:

(79) $$\boldsymbol{\psi}_{emp}(\boldsymbol{x}_r, \tau) \to \langle \boldsymbol{\psi}_{emp}(\boldsymbol{x}_r, \tau) \rangle \text{ as } T \to \infty.$$

Proposition 5 is the electromagnetic analogue of a statistical stability result for scalar waves that was proven originally in [28] (see also [8]) and is proved in Appendix A.

7. NUMERICAL EXPERIMENTS

We illustrate the proposed imaging method with numerical experiments in a regime corresponding to microwaves propagating in vacuum (section 7.1). We start in section 7.3 with experiments where the data is the coherency matrix over a certain bandwidth (as defined in section 2). We refer to these experiments as deterministic, because no empirical averaging is performed. We investigate the behavior of the imaging routine for a few dipole scatterers, as well as for an extended scatterer. The visualization of the 2×2 projected polarizability tensors that appear in our images is explained in section 7.2. We then report in section 7.4 an experiment with the electric dipole source being driven by a time domain Gaussian process and the measured data are the empirical correlations (77).
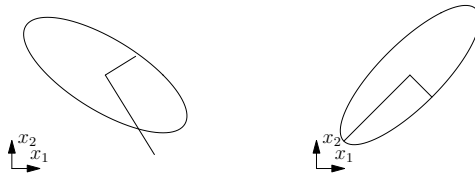
FIGURE 4. Sample visualization using ellipses for a non-symmetric matrix $\boldsymbol{A}_1$ (left) and a symmetric matrix $\boldsymbol{A}_2$ (right), as defined in (80). The ellipses have been normalized so that the longest principal axes have the same length. The departure of the vectors from the principal axes indicates a non-symmetric matrix.

7.1. **Physical parameters.** In all of our experiments, we assume a homogeneous background medium with wave speed given by that of light in vacuum, i.e., $c = (\varepsilon\mu)^{-1/2} = 3 \times 10^8$ ms^{-1}. We use the central frequency $\omega_0/(2\pi) = 2.4$ GHz, which gives a central wavelength of $\lambda_0 = 0.125$ m. Our receiver array consists of 61×61 receivers located at the points $\mathcal{A} = \{(u_i, v_j, 0) : u_i = i(20\lambda_0/61), v_j = j(20\lambda_0/61), i, j = -30, \ldots, 30\}$. This corresponds to a square array of side $a = 20\lambda_0$ in the $x_3 = 0$ plane, centered at the origin, consisting of 61×61 uniformly spaced receivers. We consider a characteristic propagation distance of $L = 100\lambda_0$, and place a single point source at the location $\boldsymbol{x}_s = (L/2, 0, L(1 - \sqrt{3/4}))$. This corresponds to a point source located on the $x_2 = 0$ plane, at a distance L from the reference point $\boldsymbol{y}_0 = (0, 0, L)$ and the source is outside of the region $\mathcal{R}(3)$ defined in (20). All of the scatterers we consider are located near $\boldsymbol{y}_0$, so we recover Kirchhoff images for points $\boldsymbol{y}$ within the cube of side $30\lambda_0$ centered at $\boldsymbol{y}_0$, i.e.,

$$\mathcal{W} = \{\boldsymbol{y} \in \mathbb{R}^3 : \|\boldsymbol{y} - \boldsymbol{y}_0\|_\infty \leq 15\lambda_0\}.$$

7.2. **Matrix visualization convention.** Recall that the imaging method of section 3 only recovers a 2×2 projection of the 3×3 complex polarizability tensor. The recovered polarizability tensor is not symmetric in general (it is symmetric for the collocated sources and receivers case [18]). We visualize matrices $\boldsymbol{A} \in \mathbb{R}^{2 \times 2}$ with the ellipse $\mathcal{E}(\boldsymbol{A}) = \{\boldsymbol{A}\boldsymbol{v} \mid \|\boldsymbol{v}\|_2 = 1\}$. To emphasize that the matrices we recover are not symmetric, we also display (when possible) the vectors $\sigma_1\boldsymbol{v}_1$ and $\sigma_2\boldsymbol{v}_2$, where we have used the singular values σ_j and right singular vectors $\boldsymbol{v}_j$, $j = 1, 2$, from the SVD $\boldsymbol{A} = [\boldsymbol{u}_1\boldsymbol{u}_2]\operatorname{diag}(\sigma_1, \sigma_2)[\boldsymbol{v}_1^T\boldsymbol{v}_2^T]$. Indeed, if the matrix $\boldsymbol{A}$ is symmetric then $\boldsymbol{v}_j = \boldsymbol{u}_j$ (up to a sign) so the vectors $\sigma_1\boldsymbol{v}_1$ and $\sigma_2\boldsymbol{v}_2$ would coincide with the principal axes of the ellipse $\mathcal{E}(\boldsymbol{A})$. An example of the visualization is presented in fig. 4 for the matrices

$$(80) \qquad \boldsymbol{A}_1 = \begin{bmatrix} 1 & -1 \\ 0 & 1 \end{bmatrix} \text{ and } \boldsymbol{A}_2 = \begin{bmatrix} 1 & 2 \\ 2 & 1 \end{bmatrix}.$$

Finally we note that the ellipses we display in all the following figures are normalized to an appropriate size, and that when the matrix $\boldsymbol{A}$ is complex, we simply visualize its real and imaginary part separately, using the same convention.

7.3. **Deterministic experiments.** For each $\boldsymbol{x}_r \in \mathcal{A}$ and for 501 uniformly spaced frequencies in the frequency band $\mathcal{B}/(2\pi) = [1.2, 3.6]$ GHz, we generate coherency

matrix data $\mathbf{\Psi}(\boldsymbol{x}_r; \omega)$ using formula (11) with a constant source coherency matrix

$$\widetilde{\boldsymbol{J}}_s(\omega) \equiv \begin{bmatrix} 1 & 0 \\ 0 & 1 \end{bmatrix}.$$

Using (16), we preprocess the data for each $\boldsymbol{x}_r \in \mathcal{A}$ and $\omega \in \mathcal{B}$ to recover the array response tensor $\boldsymbol{p}(\mathbf{\Psi})(\boldsymbol{x}_r, \boldsymbol{x}_s; k)$, and then compute the Kirchhoff imaging function $\mathcal{I}_{KM}[\boldsymbol{p}(\mathbf{\Psi})](\boldsymbol{y}; \omega/c)$ for each $\boldsymbol{y}$ in the imaging window $\mathcal{W}$. Reconstruction of the projected polarizability tensor $\widetilde{\boldsymbol{\alpha}}(\boldsymbol{y})$ is performed by integrating $\widetilde{\boldsymbol{\alpha}}(\boldsymbol{y}; \omega)$ over the frequency band $\mathcal{B}$ (as in (67)), where we recover $\widetilde{\boldsymbol{\alpha}}(\boldsymbol{y}; \omega)$ using a slightly different formula (see remark 6):

$$(81) \qquad \widetilde{\boldsymbol{\alpha}}(\boldsymbol{y}; \omega) = \left(\boldsymbol{U}_\parallel^* \boldsymbol{H}_r(\boldsymbol{y}, \boldsymbol{y}; k) \boldsymbol{U}_\parallel \right)^{-1} \widetilde{\mathcal{I}}_{KM}(\boldsymbol{y}; \omega/c) \left(\boldsymbol{U}_s^* \boldsymbol{H}_s(\boldsymbol{y}, \boldsymbol{y}; k) \boldsymbol{U}_s \right)^{-1}.$$

Finally, we perform the phase correction described in section 5.6.

For our first experiment, we consider three dipole scatterers located at $\boldsymbol{y}_1 = (-6\lambda_0, -5\lambda_0, 100\lambda_0)$, $\boldsymbol{y}_2 = (7\lambda_0, -5\lambda_0, 100\lambda_0)$, and $\boldsymbol{y}_3 = (5\lambda_0, 8\lambda_0, 106\lambda_0)$, with respective polarizability tensors

$$(82) \qquad \boldsymbol{\alpha}_1 = \begin{bmatrix} 2 + \imath & -\imath & 1 \\ -\imath & 1 + 2\imath & \imath \\ 1 & \imath & 1 + \imath \end{bmatrix}, \quad \boldsymbol{\alpha}_2 = \begin{bmatrix} 2 + 2\imath & -1 + \imath & \imath/2 \\ -1 + \imath & 1 + 2\imath & 0 \\ \imath/2 & 0 & 1 \end{bmatrix},$$
$$\boldsymbol{\alpha}_3 = \begin{bmatrix} 2 - 2\imath & 1 + \imath & 0 \\ 1 + \imath & 1 + 2\imath & (1 - \imath)/2 \\ 0 & (1 - \imath)/2 & \imath \end{bmatrix}.$$

Figure 5 compares cross-range images formed from the true array response $\mathbf{\Pi}$ and the recovered array response $\boldsymbol{p}(\mathbf{\Psi})$, at the range locations $x_3 = 100\lambda_0$ and $x_3 = 106\lambda_0$. The colormap indicates the Frobenius norm of the recovered polarizability tensor $\|\widetilde{\boldsymbol{\alpha}}(\boldsymbol{y})\|_F$ at each image point $\boldsymbol{y}$. The true polarizability tensor norms are given by $\|\widetilde{\boldsymbol{\alpha}}_1\|_F \approx 3.44, \|\widetilde{\boldsymbol{\alpha}}_2\|_F \approx 3.93, \|\widetilde{\boldsymbol{\alpha}}_3\|_F \approx 3.82$, thus we observe accurate recovery of the norm. Meanwhile, the ellipses/axes depict the 2×2 tensors $\widetilde{\boldsymbol{\alpha}}_i$ at the exact scatterer locations $\boldsymbol{y}_i$. We use solid white (resp. dashed black) and solid yellow (resp. dashed magenta) ellipses/axes for the real and imaginary parts of the true (resp. recovered) tensor $\widetilde{\boldsymbol{\alpha}}_i$, using the visualization convention in section 7.2. Both true and recovered tensor are displayed with the phase correction in section 5.6. In a similar fashion, fig. 6 compares range images at the cross-range locations $x_2 = -5\lambda_0$ and $x_2 = 8\lambda_0$. In both figures, the images are essentially indistinguishable.

Next, we demonstrate the oscillatory artifacts in the recovery of the projected polarizability tensor $\widetilde{\boldsymbol{\alpha}}(\boldsymbol{y})$ and their correction, as explained in section 5.6. In fig. 7(a), we show a cross-range image of the recovered tensor field $\widetilde{\boldsymbol{\alpha}}(\boldsymbol{y})$ near the scatterer location $\boldsymbol{y}_1 = (-6\lambda_0, -5\lambda_0, 100\lambda_0)$. We use the convention of section 7.2 to represent with ellipses the projected polarizability tensor $\widetilde{\boldsymbol{\alpha}}(\boldsymbol{y})$, but omit the axes representing the right singular vectors to avoid over-cluttering the image. The ellipses all have the same longest principal axis and their color corresponds to $\|\widetilde{\boldsymbol{\alpha}}(\boldsymbol{y})\|_F$. We immediately notice that the tensor oscillates wildly away from the scatterer position, which confirms the analysis of section 5.6. In fig. 7(b), we visualize the tensor field $\overline{\widetilde{\alpha}_{1,1}(\boldsymbol{y})}/|\widetilde{\alpha}_{1,1}(\boldsymbol{y})|\widetilde{\boldsymbol{\alpha}}(\boldsymbol{y})$ in a similar fashion. This imposes that $\widetilde{\alpha}_{1,1}(\boldsymbol{y})$ be real. The images in range for the same scatterer located at $\boldsymbol{y}_1$ appear in fig. 8. Oscillatory artifacts are present away from the scatterer location and are suppressed using the same method.
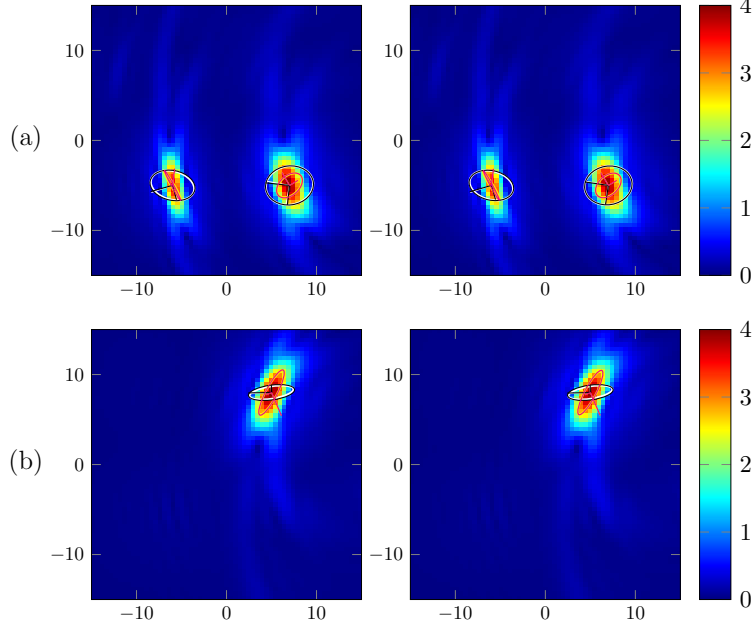
FIGURE 5. Dipole scatterers: cross-range images of $\|\widetilde{\boldsymbol{\alpha}}(\boldsymbol{y})\|_F$ at range locations (a) $x_3 = 100\lambda_0$ and (b) $x_3 = 106\lambda_0$. The left and right columns show reconstructions from the true array response $\boldsymbol{\Pi}$ and the recovered array response $\boldsymbol{p}(\boldsymbol{\Psi})$, respectively. Here the true tensor $\mathrm{Re}(\widetilde{\alpha}_{1,1}/|\widetilde{\alpha}_{1,1}|\widetilde{\boldsymbol{\alpha}})$ (resp. $\mathrm{Im}(\widetilde{\alpha}_{1,1}/|\widetilde{\alpha}_{1,1}|\widetilde{\boldsymbol{\alpha}})$) is depicted by the white (resp. yellow) ellipses/axes. Similarly, the recovered tensor is depicted using black (real) and magenta (imaginary) ellipses/axes.

As a final deterministic experiment, we consider an extended scatterer. For simplicity we choose a cube of side $5\lambda_0$ centered at $(0, 0, 100\lambda_0)$. We simulate this scatterer using a collection of dipole scatterers separated by $\lambda_0/4$, each with polarizability tensor

$$\boldsymbol{\alpha}_0 = \begin{bmatrix} 2 - \imath & 3 + 2\imath & 0 \\ 3 + 2\imath & -1 & 0 \\ 0 & 0 & 1 \end{bmatrix}.$$

We visualize $\|\widetilde{\boldsymbol{\alpha}}(\boldsymbol{y})\|_F$ in cross-range and range in fig. 9(a) and fig. 9(b) respectively, where the outline of the true scatterer is indicated in cyan. In the range image we find that the Kirchhoff imaging routine only resolves discontinuities in the medium wave speed, while the interior of the cube is not accurately recovered. This is similar to what happens in acoustics, see e.g. [11]. In fig. 10, we visualize the corresponding tensor field with suppressed oscillatory artifacts $\overline{\widetilde{\alpha}_{1,1}(\boldsymbol{y})}/|\widetilde{\alpha}_{1,1}(\boldsymbol{y})|\widetilde{\boldsymbol{\alpha}}(\boldsymbol{y})$.

From the experiments in this section, we confirm that combining theorem 1 and proposition 4, one obtains a good reconstruction of $\widetilde{\boldsymbol{\alpha}}$ using only coherency matrix data $\boldsymbol{p}(\boldsymbol{\Psi})$. On one hand, theorem 1 tells us that $\mathcal{I}_{KM}[\boldsymbol{p}(\boldsymbol{\Psi})](\boldsymbol{y}; \omega/c)$ is asymptotically close to $\mathcal{I}_{KM}[\boldsymbol{U}_\parallel \widetilde{\boldsymbol{\Pi}} \boldsymbol{U}_s^*](\boldsymbol{y}; \omega/c) = \mathcal{I}_{KM}[\boldsymbol{P}_\parallel \boldsymbol{\Pi} \boldsymbol{P}_s](\boldsymbol{y}; \omega/c)$ if the frequency is
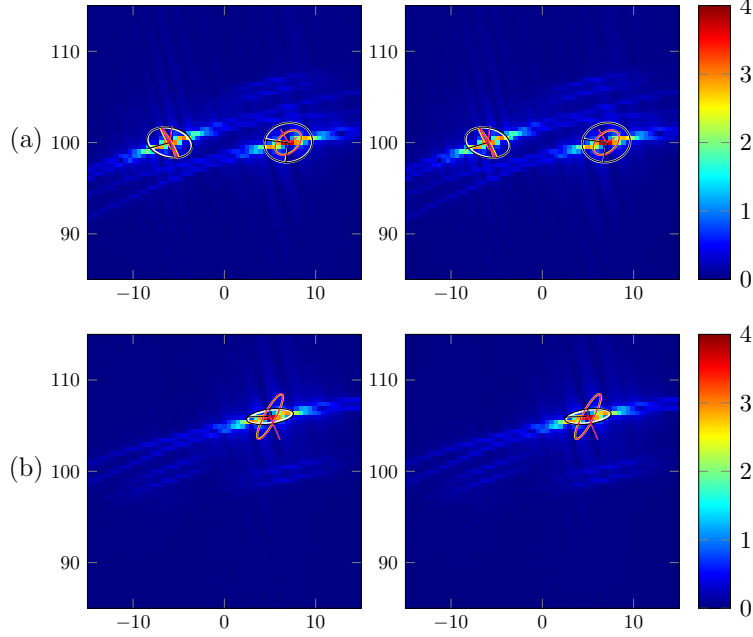
FIGURE 6. Dipole scatterers: range images of $\|\widetilde{\boldsymbol{\alpha}}(\boldsymbol{y})\|_F$ at cross-range locations (a) $x_2 = -5\lambda_0$ and (b) $x_2 = 8\lambda_0$. The left and right columns show reconstructions from the true array response $\boldsymbol{\Pi}$ and the recovered array response $\boldsymbol{p}(\boldsymbol{\Psi})$, respectively. Here the true tensor $\mathrm{Re}(\widetilde{\alpha}_{1,1}/|\widetilde{\alpha}_{1,1}|\widetilde{\boldsymbol{\alpha}})$ (resp. $\mathrm{Im}(\widetilde{\alpha}_{1,1}/|\widetilde{\alpha}_{1,1}|\widetilde{\boldsymbol{\alpha}})$) is depicted by the white (resp. yellow) ellipses/axes. Similarly, the recovered tensor is depicted using black (real) and magenta (imaginary) ellipses/axes.

sufficiently high. On the other hand, in the Fraunhofer regime, proposition 4 tells us that both images $\mathcal{I}_{KM}[\boldsymbol{P}_\parallel \boldsymbol{\Pi} \boldsymbol{P}_s](\boldsymbol{y}; \omega/c)$ (with incomplete polarization data) and $\mathcal{I}_{KM}[\boldsymbol{\Pi}](\boldsymbol{y}; \omega/c)$ (with full data) have the same asymptotic expansion. Thus, by post-processing $\mathcal{I}_{KM}[\boldsymbol{P}_\parallel \boldsymbol{\Pi} \boldsymbol{P}_s](\boldsymbol{y}; \omega/c)$ (according to relations (67), (55), and correction of the oscillatory artifacts explained in section 5.6), one obtains a good reconstruction of the position and polarizability tensor $\widetilde{\boldsymbol{\alpha}}$ of each dipole with the same resolution (both in cross-range and range) as in the full data case.

Remark 5. *Note that the decay of the cross-range Kirchhoff images as we move away from the scatterers (figs. 5 to 8) is slower than the decay that was observed for the collocated sources and receivers array case in [18]. The decay of the images in our case is given by propositions 2 and 3 and is inversely proportional to the cross-range distance from a scatterer to the imaging point. For the collocated sources and receiver case, the decay is inversely proportional to the distance squared.*

Remark 6. *We use (81) instead of (55) to recover $\widetilde{\boldsymbol{\alpha}}(\boldsymbol{y}; \omega)$ for each $\omega \in \mathcal{B}$. However, the reconstruction formulas (81) and (55) are asymptotically close since (55) amounts to using the Fraunhofer asymptotic of $\boldsymbol{U}_\parallel^* \boldsymbol{H}_r(\boldsymbol{y}, \boldsymbol{y}; k) \boldsymbol{U}_\parallel$ and $\boldsymbol{U}_s^* \boldsymbol{H}_s(\boldsymbol{y}, \boldsymbol{y}; k) \boldsymbol{U}_s$*
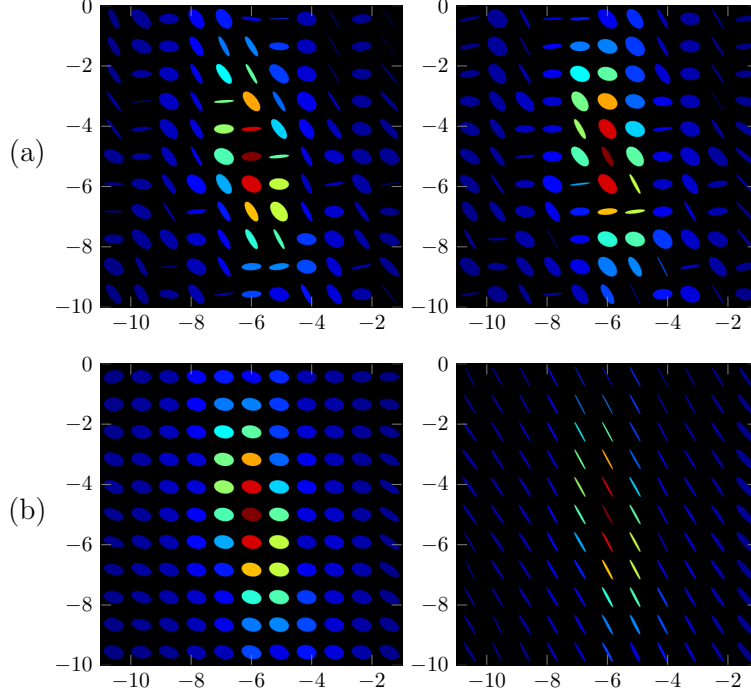
FIGURE 7. Cross-range visualization of the recovered tensor field $\widetilde{\boldsymbol{\alpha}}(\boldsymbol{y})$ near $(-6\lambda_0, -5\lambda_0, 100\lambda_0)$. Row (a) shows the tensor field $\widetilde{\boldsymbol{\alpha}}$ with oscillatory artifacts, while row (b) shows the field $\overline{\widetilde{\alpha}_{1,1}}/|\widetilde{\alpha}_{1,1}|\widetilde{\boldsymbol{\alpha}}$ with suppressed oscillatory artifacts. The left and right columns show the real and imaginary parts of the tensors, respectively.

to reconstruct $\widetilde{\boldsymbol{\alpha}}$. Indeed, thanks to (40) and (45), one can show

$$\boldsymbol{U}_{\parallel}^* \boldsymbol{H}_r(\boldsymbol{y}, \boldsymbol{y}; k)\boldsymbol{U}_{\parallel} = \frac{\operatorname{mes}\mathcal{A}}{(4\pi L)^2}\boldsymbol{I} + \mathcal{O}\left(\frac{a^4\Theta_a}{L^4}\right) + \mathcal{O}\left(\frac{a^2\Theta_b}{L^2}\right) + \mathcal{O}\left(\frac{a^3}{L^3}\right),$$

$$\boldsymbol{U}_s^* \boldsymbol{H}_s(\boldsymbol{y}, \boldsymbol{y}; k)\boldsymbol{U}_s = \frac{1}{(4\pi L)^2}\boldsymbol{I} + O\left(\frac{b}{L}\right) + \mathcal{O}\left(\frac{a^2}{\Theta_a L^2}\right),$$

where $\boldsymbol{I}$ is the 2×2 identity. Thus, $\widetilde{\boldsymbol{\alpha}}$ reconstructed with (81) satisfies:

$$\widetilde{\boldsymbol{\alpha}}(\boldsymbol{y}; \omega) = \frac{(4\pi L)^4}{\operatorname{mes}\mathcal{A}}\widetilde{\mathcal{I}}_{KM}(\boldsymbol{y}; k) + \mathcal{O}\left(\frac{a^2\Theta_a}{L^2}\right) + \mathcal{O}\left(\Theta_b\right) + \mathcal{O}\left(\frac{a}{L}\right),$$

where the leading order term corresponds to (55). We use (81) instead of (55) as it may be more robust in other settings than the Fraunhofer asymptotic regime.

7.4. **Stochastic experiment.** Here we perform an experiment where we drive the electric dipole source at $\boldsymbol{x}_s$ using a stochastic polarization vector $\boldsymbol{j}_s(t)$. For this experiment, we use the same 3-dipole scatterer setup given in section 7.3.
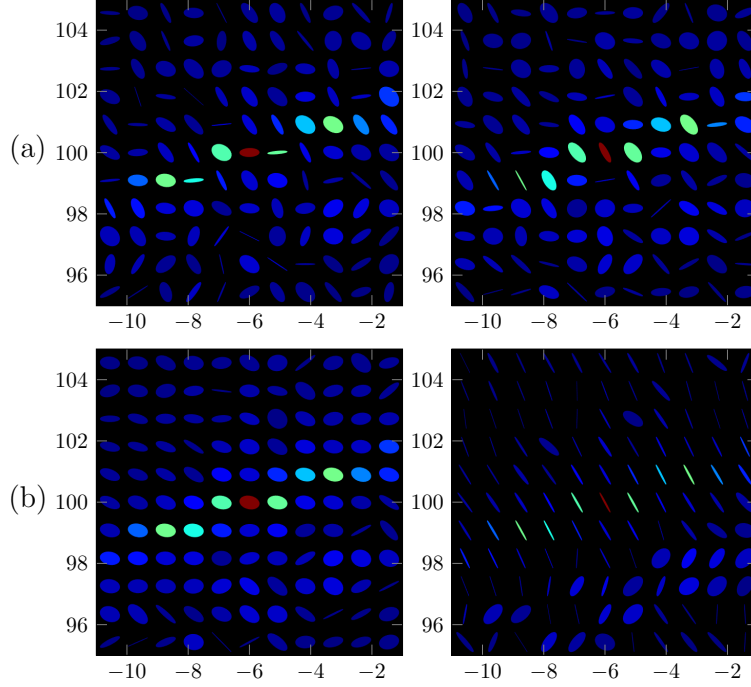
FIGURE 8. Stability: range visualization of the recovered tensor field $\widetilde{\boldsymbol{\alpha}}(\boldsymbol{y})$ near $(-6\lambda_0, -5\lambda_0, 100\lambda_0)$. Row (a) shows the tensor field $\widetilde{\boldsymbol{\alpha}}$, while row (b) shows the stabilized tensor field $\overline{\widetilde{\alpha}_{1,1}}/|\widetilde{\alpha}_{1,1}|\widetilde{\boldsymbol{\alpha}}$. The left and right columns show the real and imaginary parts of the tensors, respectively.

Making use of a vector version of the Wiener-Khinchin theorem, we generate $\boldsymbol{j}_s(t)$ as a real Gaussian process satisfying

$$(83) \qquad \langle \boldsymbol{j}_s(t) \rangle = \boldsymbol{0} \text{ and } \langle \boldsymbol{j}_s(t+\tau)\boldsymbol{j}_s(t)^T \rangle = \boldsymbol{U}_s J(\tau) \begin{bmatrix} 1 & 0 \\ 0 & 1 \end{bmatrix} \boldsymbol{U}_s^*,$$

where

$$(84) \qquad J(\tau) = 4\pi t_c^{-1} \cos(\omega_0 \tau) \exp[-\pi(\tau/t_c)^2].$$

Here t_c denotes the correlation time, which we set to $t_c \approx 1$ ns giving the signal a frequency band of roughly $\mathcal{B}/(2\pi) = [1.2, 3.6]$ GHz. We generate signals of length $2T$ for $T \approx 266$ ns with 8001 uniformly spaced samples. This sampling is sufficient to resolve frequencies in $\mathcal{B}$, while T is long enough to observe good ergodic averaging (see section 6).

We generate the electric field corresponding to $\boldsymbol{j}_s(t)$, given in the frequency domain by the first Born approximation as

$$\boldsymbol{E}(\boldsymbol{x}_r, \omega) = (\boldsymbol{G}(\boldsymbol{x}_r, \boldsymbol{x}_s; \omega/c) + \boldsymbol{\Pi}(\boldsymbol{x}_r, \boldsymbol{x}_s; \omega/c)) \, \boldsymbol{j}_s(\omega).$$

To avoid problems with circular correlation in numerics, we transform this signal to the time domain, appropriately zero-pad the result and then transform the padded
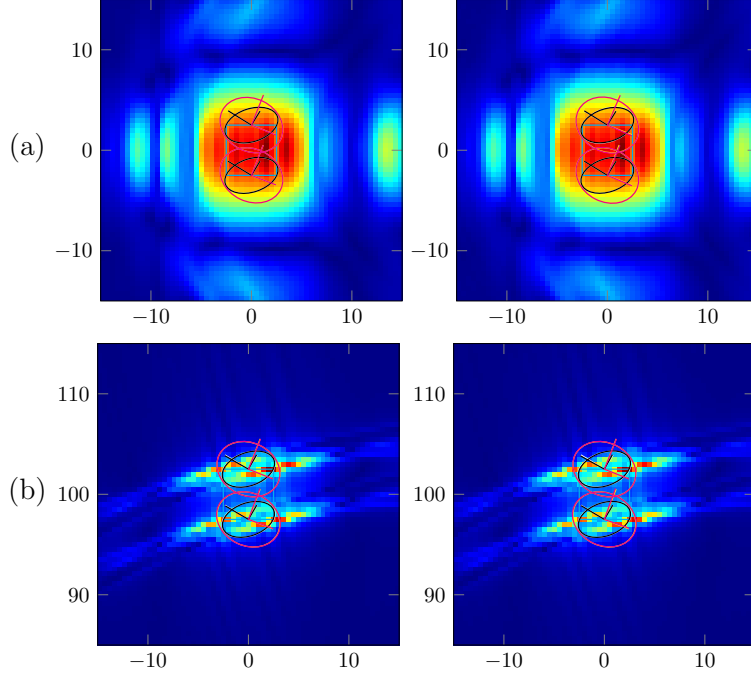
FIGURE 9. Extended scatterer (cube): visualization of $\|\widetilde{\boldsymbol{\alpha}}(\boldsymbol{y})\|_F$ in (a) cross-range at $x_3 = 100\lambda_0$ and (b) range at $x_2 = 0$. The left and right columns show reconstructions from the true array response $\boldsymbol{\Pi}$ and the recovered array response $\boldsymbol{p}(\boldsymbol{\Psi})$, respectively.

time signal back to the frequency domain (see e.g., [30, Appendix B]). Finally, the empirical correlations in (77) are generated for each $\boldsymbol{x}_r \in \mathcal{A}$ as

$$\boldsymbol{\psi}_{emp}(\boldsymbol{x}_r, \tau) = \frac{2\pi}{2T} \int d\omega e^{-i\omega\tau} \boldsymbol{U}_\|^* \boldsymbol{E}(\boldsymbol{x}_r, \omega)\overline{\boldsymbol{E}(\boldsymbol{x}_r, \omega)}^T \boldsymbol{U}_\|.$$

We preprocess the empirical correlations according to (16) to obtain $\boldsymbol{p}(\boldsymbol{\psi}_{emp})$, and then form the Kirchhoff image functions $\mathcal{I}_{KM}[\boldsymbol{p}(\boldsymbol{\psi}_{emp})](\boldsymbol{y}; k)$. The recovery of the projected polarizability tensor $\widetilde{\boldsymbol{\alpha}}(\boldsymbol{y})$ is performed as in the deterministic setting (i.e., using (81) to recover $\widetilde{\boldsymbol{\alpha}}(\boldsymbol{y}; \omega)$ followed by integration over the frequency band as in (67)).

In fig. 11, we show the cross-range images formed using the true array response $\boldsymbol{\Pi}$, and the recovered array response $\boldsymbol{p}(\boldsymbol{\psi}_{emp})$. Here we see, just as in the deterministic setting, good recovery of both the locations and tensors of each dipole scatterer $\widetilde{\boldsymbol{\alpha}}(\boldsymbol{y}_i)$. In fig. 13, we again demonstrate our proposed phase correction method and the accurate tensor recovery it provides.

8. SUMMARY AND FUTURE WORK

We have introduced a method for imaging the polarization tensor of small dielectric scatterers in a homogeneous medium, from measurements of the coherency matrix at an array arising from illumination of a point source. The main idea in
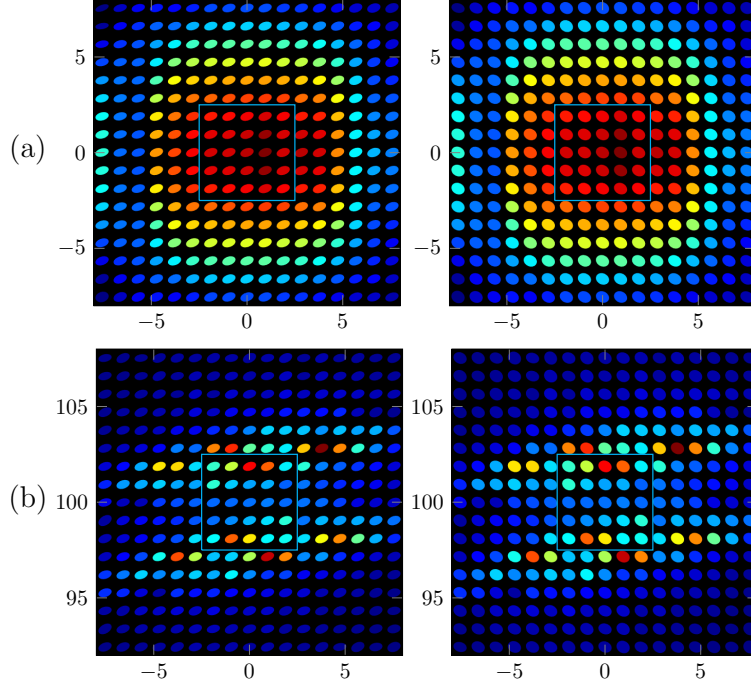
FIGURE 10. Extended scatterer (cube): visualization of the stabilized tensor field in (a) cross-range at $x_3 = 100\lambda_0$ and (b) range at $x_2 = 0$. The left column depicts $\mathrm{Re}(\overline{\widetilde{\alpha}_{1,1}}/|\widetilde{\alpha}_{1,1}|\widetilde{\boldsymbol{\alpha}})$, while the right column depicts $\mathrm{Im}(\overline{\widetilde{\alpha}_{1,1}}/|\widetilde{\alpha}_{1,1}|\widetilde{\boldsymbol{\alpha}})$.

our method is to partially recover the total electric field at the array and then use it to image using an electromagnetic version of Kirchhoff migration. We prove using a stationary phase argument that the error we make in estimating the electric field does not affect the images. Moreover the images we obtain are tensor fields that contain information about the components of the polarization tensor in a certain basis.

There are several ways in which we plan to extend this work. The first one is to study this problem when the particles are close to an interface. This is useful in microscopy, where the objects that one wishes to image are on a substrate and would involve using half-space Green functions. In the same direction, stratified media Green functions could be considered. One aspect of our method is that we are using what are essentially interference patterns between the incident and scattered fields. In this respect, our method is a form of holography. It is natural to ask whether we can use other incident fields to image (e.g. a plane wave). Finally we point out that our analysis relies on a linearization of the problem (Born approximation). In reality nearby scatterers could interact. We would like to study this case using discrete Lippmann-Schwinger models (e.g. the Foldy-Lax model [38, 19]) to find the locations of scatterers and also correct for any artifacts the multiple reflections may have introduced.
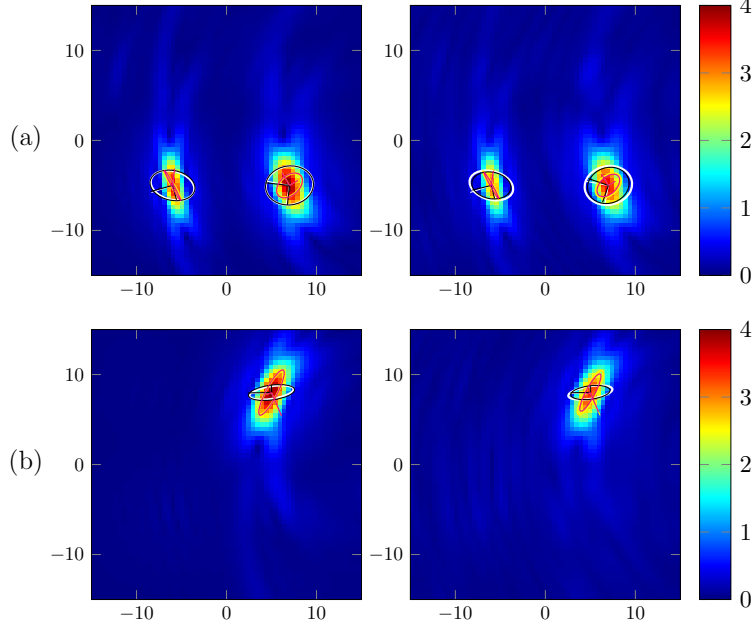
FIGURE 11. Stochastic experiment: cross-range images of $\|\widetilde{\boldsymbol{\alpha}}(\boldsymbol{y})\|_F$ at range locations (a) $x_3 = 100\lambda_0$ and (b) $x_3 = 106\lambda_0$. The left and right columns show reconstructions from the true array response $\boldsymbol{\Pi}$ and the recovered array response $\widetilde{\boldsymbol{\Pi}}$, respectively. Here the true tensor $\mathrm{Re}(\widetilde{\alpha}_{1,1}/|\widetilde{\alpha}_{1,1}|\widetilde{\boldsymbol{\alpha}})$ (resp. $\mathrm{Im}(\widetilde{\alpha}_{1,1}/|\widetilde{\alpha}_{1,1}|\widetilde{\boldsymbol{\alpha}})$) is depicted by the white (resp. yellow) ellipses/axes. Similarly, the recovered tensor is depicted using black (real) and magenta (imaginary) ellipses/axes.

APPENDIX A. PROOF OF PROPOSITION 5

Here we prove proposition 5. This proposition and its proof are patterned after a result by Garnier and Papanicolaou [28, Proposition 4.1] which was shown in the case of acoustic waves. We make the necessary modifications to adapt the result to the electromagnetic setting. Throughout this section we slightly abuse notation by identifying functions in the time domain and in the frequency domain using the same symbol.
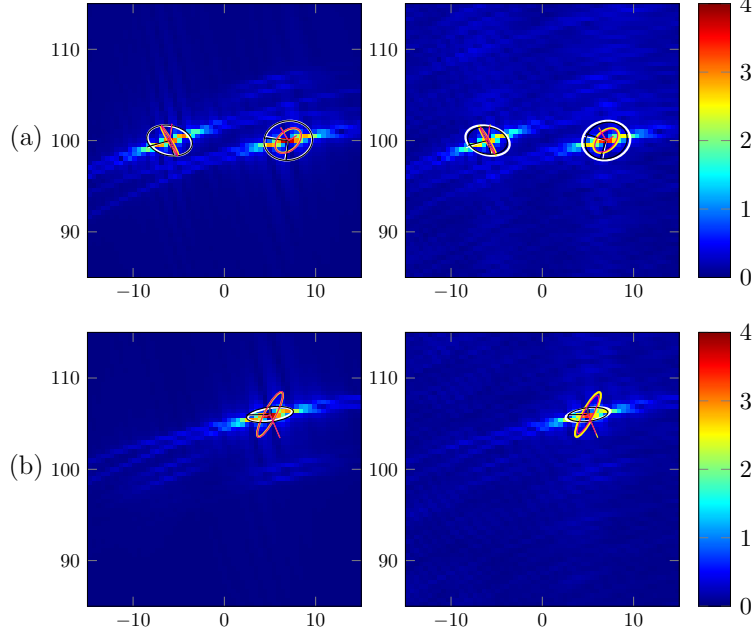
FIGURE 12. Stochastic experiment: range images of $\|\widetilde{\boldsymbol{\alpha}}(\boldsymbol{y})\|_F$ at cross-range locations (a) $x_2 = -5\lambda_0$ and (b) $x_2 = 8\lambda_0$. The left and right columns show reconstructions from the true array response $\boldsymbol{\Pi}$ and the recovered array response $\widetilde{\boldsymbol{\Pi}}$, respectively. Here the true tensor $\text{Re}(\widetilde{\alpha}_{1,1}/|\widetilde{\alpha}_{1,1}|\widetilde{\boldsymbol{\alpha}})$ (resp. $\text{Im}(\widetilde{\alpha}_{1,1}/|\widetilde{\alpha}_{1,1}|\widetilde{\boldsymbol{\alpha}})$) is depicted by the white (resp. yellow) ellipses/axes. Similarly, the recovered tensor is depicted using black (real) and magenta (imaginary) ellipses/axes.

Proof. Let us introduce the notation

$$\boldsymbol{\mathcal{G}}(\boldsymbol{x}_r, \omega) \equiv \boldsymbol{G}(\boldsymbol{x}_r, \boldsymbol{x}_s; \omega/c) + \boldsymbol{\Pi}(\boldsymbol{x}_r, \boldsymbol{x}_s; \omega/c)$$

so that the total electric field is $\boldsymbol{E}(\boldsymbol{x}_r, \omega) = \boldsymbol{\mathcal{G}}(\boldsymbol{x}_r, \omega)\boldsymbol{j}_s(\omega)$ in the frequency domain. In the time domain, the total field is

$$\boldsymbol{E}(\boldsymbol{x}_r, t) = (2\pi)^{-1}[\boldsymbol{\mathcal{G}}(\boldsymbol{x}_r, \cdot) * \boldsymbol{j}_s(\cdot)](t),$$

and is a stationary random process because we assume the process $\boldsymbol{j}_s(t)$ driving the source is stationary. Hence we have

$$\langle \boldsymbol{\psi}_{emp}(\boldsymbol{x}_r, \tau) \rangle = \frac{1}{2T} \int_{-T}^{T} dt \boldsymbol{U}_{\|}^* \left\langle \boldsymbol{E}(\boldsymbol{x}_r, t+\tau)\boldsymbol{E}(\boldsymbol{x}_r, t)^T \right\rangle \boldsymbol{U}_{\|}$$

$$= \frac{1}{2T} \int_{-T}^{T} dt \boldsymbol{U}_{\|}^* \left\langle \boldsymbol{E}(\boldsymbol{x}_r, \tau)\boldsymbol{E}(\boldsymbol{x}_r, 0)^T \right\rangle \boldsymbol{U}_{\|}$$

$$= \boldsymbol{U}_{\|}^* \left\langle \boldsymbol{E}(\boldsymbol{x}_r, \tau)\boldsymbol{E}(\boldsymbol{x}_r, 0)^T \right\rangle \boldsymbol{U}_{\|},$$
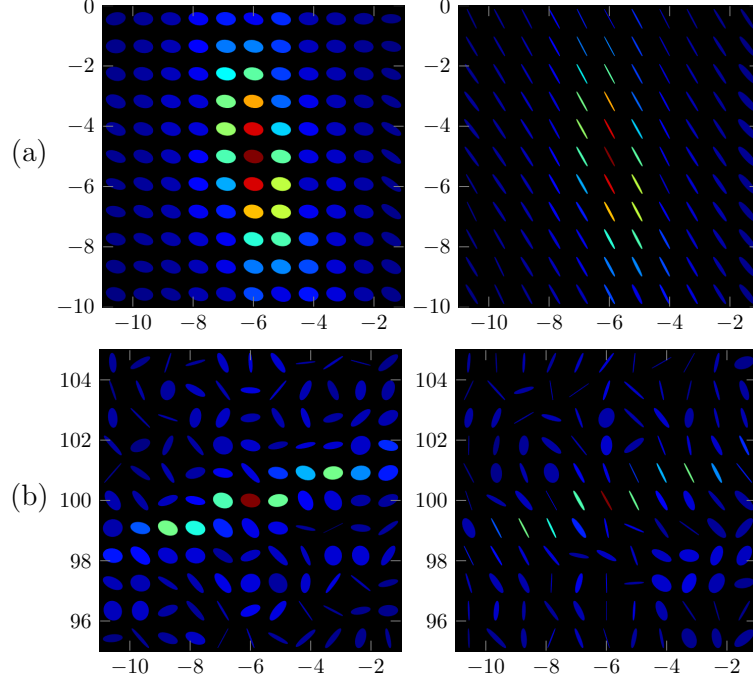
FIGURE 13. Stochastic experiment: visualization of the tensor field with suppressed oscillatory artifacts in (a) cross-range and (b) range, near the location $\boldsymbol{y} = (-6\lambda_0, -5\lambda_0, 100\lambda_0)$. The left column depicts $\mathrm{Re}(\widetilde{\overline{\alpha}_{1,1}}|\widetilde{\alpha}_{1,1}|\widetilde{\boldsymbol{\alpha}})$, while the right column depicts $\mathrm{Im}(\widetilde{\overline{\alpha}_{1,1}}|\widetilde{\alpha}_{1,1}|\widetilde{\boldsymbol{\alpha}})$.

and thus $\langle \boldsymbol{\psi}_{emp}(\boldsymbol{x}_r, \tau) \rangle$ is independent of T. Furthermore, we have

$$
\begin{aligned}
\langle \boldsymbol{E}(\boldsymbol{x}_r, \tau) \boldsymbol{E}(\boldsymbol{x}_r, 0)^T \rangle &= \int dt' \int dt'' \boldsymbol{\mathcal{G}}(\boldsymbol{x}_r, \tau - t') \langle \boldsymbol{j}_s(t') \boldsymbol{j}_s(t'')^T \rangle \boldsymbol{\mathcal{G}}(\boldsymbol{x}_r, -t'')^T \\
&= \int dt' \int dt'' \boldsymbol{\mathcal{G}}(\boldsymbol{x}_r, \tau - t') \boldsymbol{U}_s \widetilde{\boldsymbol{J}}_s(t' - t'') \boldsymbol{U}_s^* \boldsymbol{\mathcal{G}}(\boldsymbol{x}_r, -t'')^T \\
&= \int dt'' \left[\boldsymbol{\mathcal{G}}(\boldsymbol{x}_r, \cdot) * \boldsymbol{U}_s \widetilde{\boldsymbol{J}}_s \boldsymbol{U}_s^* \right] (\tau - t'') \boldsymbol{\mathcal{G}}(\boldsymbol{x}_r, -t'')^T \\
&= (2\pi) \int d\omega e^{-\imath \omega \tau} \boldsymbol{\mathcal{G}}(\boldsymbol{x}_r, \omega) \boldsymbol{U}_s \widetilde{\boldsymbol{J}}_s(\omega) \boldsymbol{U}_s^* \boldsymbol{\mathcal{G}}(\boldsymbol{x}_r, \omega)^*.
\end{aligned}
$$

Equation (78) is verified by multiplying the previous expression on the left by $\boldsymbol{U}_\parallel^*$ and on the right by $\boldsymbol{U}_\parallel$.

We show the ergodicity in (79), by proving that the variance of each component of $\boldsymbol{\psi}_{emp}(\boldsymbol{x}_r, \tau)$ is $\mathcal{O}(1/T)$ as $T \to \infty$. To simplify the expressions we use the notations $[(\boldsymbol{\psi}_{emp})(\boldsymbol{x}_r, t)]_{ij} = \psi_{ij}(t)$, $[\boldsymbol{\mathcal{G}}(\boldsymbol{x}_r, t)]_{mn} = \mathcal{G}_{mn}(t)$, $[\boldsymbol{J}_s(t)]_{mn} = J_{mn}(t)$ and $[\boldsymbol{j}_s(t)]_m = j_m(t)$ for $i, j \in \{1, 2\}$ and $m, n \in \{1, 2, 3\}$. We compute the covariance

of $\psi_{ij}(\tau)$ with the Einstein summation convention,

$$
\text{Cov}\big(\psi_{ij}(\tau), \psi_{i'j'}(\tau + \Delta\tau)\big) = \frac{1}{(2T)^2} \int_{-T}^{T} \int_{-T}^{T} dt dt' \int ds ds' du du'
$$

(85)
$$
\times \, \mathcal{G}_{im}(s + \tau)\mathcal{G}_{jn}(u)\mathcal{G}_{i'm'}(s' + \tau + \Delta\tau)\mathcal{G}_{j'n'}(u')
$$
$$
\times \Big[\langle j_m(t - s)j_n(t - u)j_{m'}(t' - s')j_{n'}(t' - u')\rangle
$$
$$
- \langle j_m(t - s)j_n(t - u)\rangle \, \langle j_{m'}(t' - s')j_{n'}(t' - u')\rangle \Big].
$$

For the following, it is helpful to notice the symmetry $J_{ij}(\tau) = J_{ji}(-\tau)$ in the time domain, which follows from (76). The product of the second order moments is

$$
\langle j_m(t - s)j_n(t - u)\rangle \, \langle j_{m'}(t' - s')j_{n'}(t' - u')\rangle = J_{mn}(u - s)J_{n'm'}(s' - u'),
$$

while the fourth order moment is given by the Gaussian moment theorem

$$
\langle j_m(t - s)j_n(t - u)j_{m'}(t' - s')j_{n'}(t' - u')\rangle = J_{mn}(u - s)J_{n'm'}(s' - u')
$$
$$
+ J_{mm'}(t - s - t' + s')J_{n'n}(t' - u' - t + u)
$$
$$
+ J_{mn'}(t - s - t' + u')J_{m'n}(t' - s' - t + u).
$$

We evaluate the following integrals as

$$
I_1 = \frac{1}{(2T)^2} \int_{-T}^{T} dt \int_{-T}^{T} dt' \, J_{mm'}(t - t' + s' - s)J_{n'n}(t' - t + u - u')
$$
$$
= \int d\omega \int d\omega' \, \text{sinc}^2((\omega - \omega')T)e^{-i\omega(s'-s)}e^{-i\omega'(u-u')}J_{mm'}(\omega)J_{n'n}(\omega'),
$$

and

$$
I_2 = \frac{1}{(2T)^2} \int_{-T}^{T} dt \int_{-T}^{T} dt' \, J_{mn'}(t - t' + u' - s)J_{m'n}(t' - t + u - s')
$$
$$
= \int d\omega \int d\omega' \, \text{sinc}^2((\omega - \omega')T)e^{-i\omega(u'-s)}e^{-i\omega'(u-s')}J_{mn'}(\omega)J_{m'n}(\omega').
$$

To see where I_1 and I_2 come from, consider that for functions f, g and scalars a, b we have

$$
\frac{1}{(2T)^2} \int_{-T}^{T} dt \int_{-T}^{T} dt' f(t - t' + a)g(t' - t + b)
$$
$$
= \frac{1}{(2T)^2} \int_{-T}^{T} dt \int_{-T}^{T} dt' \int d\omega e^{-i\omega(t-t'+a)} f(\omega) \int d\omega' e^{-i\omega'(t'-t+b)} g(\omega')
$$
$$
= \frac{1}{(2T)^2} \int d\omega \int d\omega' f(\omega)g(\omega')e^{-i\omega a}e^{-i\omega' b} \int_{-T}^{T} dt e^{it(\omega'-\omega)} \int_{-T}^{T} dt' e^{it'(\omega-\omega')}
$$
$$
= \int d\omega \int d\omega' f(\omega)g(\omega')e^{-i\omega a}e^{-i\omega' b} \left(\frac{\sin(T(\omega' - \omega))}{T(\omega' - \omega)}\right)^2.
$$

We split the covariance (85) into two terms $\text{Cov}(\psi_{ij}(\tau), \psi_{i'j'}(\tau + \Delta\tau)) = V_1 + V_2$, where V_l involves I_l, $l = 1, 2$. Using the expression for I_1 in the first term V_1, we

can evaluate the integrals in s, s', u, u' to get

$$V_1 = \int ds ds' du du' \mathcal{G}_{im}(s+\tau) \mathcal{G}_{jn}(u) \mathcal{G}_{i'm'}(s'+\tau+\Delta\tau) \mathcal{G}_{j'n'}(u') I_1$$

$$= (2\pi)^4 \int d\omega \int d\omega' e^{i\omega\Delta\tau} \operatorname{sinc}^2((\omega-\omega')T) \mathcal{G}_{im}(\omega) \mathcal{G}_{i'm'}(-\omega) \mathcal{G}_{jn}(-\omega') \mathcal{G}_{j'n'}(\omega')$$

$$\times J_{mm'}(\omega) J_{n'n}(\omega').$$

The details for the calculation of V_1 are as follows,

$$\int ds e^{i\omega s} \mathcal{G}_{im}(s+\tau) = (2\pi) e^{-i\omega\tau} \mathcal{G}_{im}(\omega),$$

$$\int ds' e^{-i\omega s'} \mathcal{G}_{i'm'}(s'+\tau+\Delta\tau) = (2\pi) e^{i\omega(\tau+\Delta\tau)} \mathcal{G}_{i'm'}(-\omega),$$

$$\int du e^{-i\omega' u} \mathcal{G}_{jn}(u) = (2\pi) \mathcal{G}_{jn}(-\omega'), \text{ and}$$

$$\int du' e^{i\omega' u'} \mathcal{G}_{j'n'}(u') = (2\pi) \mathcal{G}_{j'n'}(\omega').$$

Similarly for the second term V_2 we obtain

$$V_2 = (2\pi)^4 \int d\omega \int d\omega' e^{-i\omega\tau} e^{-i\omega'(\tau+\Delta\tau)} \operatorname{sinc}^2((\omega-\omega')T)$$

$$\times \mathcal{G}_{im}(\omega) \mathcal{G}_{i'm'}(\omega') \mathcal{G}_{jn}(-\omega') \mathcal{G}_{j'n'}(-\omega) J_{mn'}(\omega) J_{m'n}(\omega').$$

The details for the calculation of V_2 are as follows,

$$\int ds e^{i\omega s} \mathcal{G}_{im}(s+\tau) = (2\pi) e^{-i\omega\tau} \mathcal{G}_{im}(\omega),$$

$$\int ds' e^{i\omega' s'} \mathcal{G}_{i'm'}(s'+\tau+\Delta\tau) = (2\pi) e^{-i\omega'(\tau+\Delta\tau)} \mathcal{G}_{i'm'}(\omega'),$$

$$\int du e^{-i\omega' u} \mathcal{G}_{jn}(u) = (2\pi) \mathcal{G}_{jn}(-\omega'), \text{ and}$$

$$\int du' e^{-i\omega u'} \mathcal{G}_{j'n'}(u') = (2\pi) \mathcal{G}_{j'n'}(-\omega).$$

Since we have

$$T \int \operatorname{sinc}^2(T\omega) d\omega = \pi,$$

we see that when we take $\Delta\tau = 0$ and the limit as $T \to \infty$ we get

$$\frac{T}{\pi} V_1 \to L_1 \equiv (2\pi)^4 \int d\omega \mathcal{G}_{im}(\omega) \mathcal{G}_{i'm'}(-\omega) \mathcal{G}_{jn}(-\omega) \mathcal{G}_{j'n'}(\omega) J_{mm'}(\omega) J_{n'n}(\omega), \text{ and}$$

$$\frac{T}{\pi} V_2 \to L_2 \equiv (2\pi)^4 \int d\omega e^{-2i\omega\tau} \mathcal{G}_{im}(\omega) \mathcal{G}_{i'm'}(\omega) \mathcal{G}_{jn}(-\omega) \mathcal{G}_{j'n'}(-\omega) J_{mn'}(\omega) J_{m'n}(\omega),$$

using an approximate Dirac identity, which we can use e.g. when $J_{ij}(\omega)$ is Schwartz class. Notice that the limiting values L_1 and L_2 are guaranteed to be real because they involve the Fourier transform of functions of ω that satisfy an appropriate reflection principle. Evaluating $\operatorname{Cov}(\psi_{ij}(t), \psi_{i'j'}(t))$ on the diagonal (i.e., $i = i', j = j'$), we conclude that $T \operatorname{Var}(\psi_{ij}(\tau)) = \mathcal{O}(1)$ as $T \to \infty$, which establishes (79). $\square$

APPENDIX B. CONDITIONING OF PROJECTED GREEN FUNCTION MATRIX

Here we show that the matrix $\boldsymbol{P}_{\parallel}\boldsymbol{G}(\boldsymbol{x}_r, \boldsymbol{x}_s; k)\boldsymbol{P}_s$ is close to a rank 2 matrix for which the condition number can be calculated explicitly in terms of the angles of the triangle spanned by $\boldsymbol{x}_r$, $\boldsymbol{x}_s$ and $\boldsymbol{y}_0$. We recall that the condition number of a rank r matrix $\boldsymbol{A}$ is $\mathrm{cond}(\boldsymbol{A}) = \sigma_1(\boldsymbol{A})/\sigma_r(\boldsymbol{A})$, where $\sigma_j(\boldsymbol{A})$ is the $j-$th singular value of $\boldsymbol{A}$. Since $\widetilde{\boldsymbol{G}}(\boldsymbol{x}_r, \boldsymbol{x}_s; k) = \boldsymbol{U}_{\parallel}^*\boldsymbol{G}(\boldsymbol{x}_r, \boldsymbol{x}_s; k)\boldsymbol{U}_s$ this result implies $\widetilde{\boldsymbol{G}}(\boldsymbol{x}_r, \boldsymbol{x}_s; k)$ is close to a 2×2 invertible matrix, because $\boldsymbol{P}_{\parallel} = \boldsymbol{U}_{\parallel}\boldsymbol{U}_{\parallel}^*$ and $\boldsymbol{P}_s = \boldsymbol{P}(\boldsymbol{x}_s, \boldsymbol{y}_0) = \boldsymbol{U}_s\boldsymbol{U}_s^*$, with the 3×2 matrices $\boldsymbol{U}_{\parallel}$ and $\boldsymbol{U}_s$ being unitary.

Lemma 2. *Under the Fraunhofer asymptotic regime (see section 5) we have that*
(86)
$$\boldsymbol{P}_{\parallel}\boldsymbol{G}(\boldsymbol{x}_r, \boldsymbol{x}_s; k)\boldsymbol{P}_s = G(\boldsymbol{x}_s, \boldsymbol{x}_r; k)\left[\boldsymbol{P}(\boldsymbol{x}_r, \boldsymbol{y}_0)\boldsymbol{P}(\boldsymbol{x}_s, \boldsymbol{x}_r)\boldsymbol{P}_s + \mathcal{O}\left(\frac{a}{L}\right) + \mathcal{O}\left(\frac{1}{kd}\right)\right].$$

Note that we neglected $\mathcal{O}(a/(kdL))$ because $kd \gg 1$ and $a/L \ll 1$. Moreover the condition number of $\boldsymbol{P}(\boldsymbol{x}_r, \boldsymbol{y}_0)\boldsymbol{P}(\boldsymbol{x}_s, \boldsymbol{x}_r)\boldsymbol{P}(\boldsymbol{y}_0, \boldsymbol{x}_s)$ is $|\cos(\theta_r)\cos(\theta_s)|^{-1}$, where θ_j is the angle at the vertex $\boldsymbol{x}_j$ of the triangle with vertices $\boldsymbol{x}_r$, $\boldsymbol{x}_s$ and $\boldsymbol{y}_0$, for $j = r, s$.

Proof. We can use [18, eq. (7)] to see that
(87)
$$\boldsymbol{G}(\boldsymbol{x}_s, \boldsymbol{x}_r; k) = G(\boldsymbol{x}_s, \boldsymbol{x}_r; k)[\boldsymbol{P}(\boldsymbol{x}_s, \boldsymbol{x}_r) + \mathcal{O}((kd)^{-1})].$$

The approximation (86) follows from the last equation and (38). To prove the expression of the condition number, we write a SVD of the projectors as follows $\boldsymbol{P}(\boldsymbol{x}_s, \boldsymbol{x}_r) = \boldsymbol{U}_{rs}\boldsymbol{U}_{rs}^*$, $\boldsymbol{P}(\boldsymbol{x}_j, \boldsymbol{y}_0) = \boldsymbol{U}_{j0}\boldsymbol{U}_{j0}^*$, where the 3×2 unitary matrices $\boldsymbol{U}_{rs}$ and $\boldsymbol{U}_{j0}$ are

(88)
$$\boldsymbol{U}_{rs} = \left[\boldsymbol{z}, \frac{\boldsymbol{z} \times (\boldsymbol{x}_r - \boldsymbol{x}_s)}{|\boldsymbol{z} \times (\boldsymbol{x}_r - \boldsymbol{x}_s)|}\right], \text{ and } \boldsymbol{U}_{j0} = \left[\boldsymbol{z}, \frac{\boldsymbol{z} \times (\boldsymbol{y}_0 - \boldsymbol{x}_j)}{|\boldsymbol{z} \times (\boldsymbol{y}_0 - \boldsymbol{x}_j)|}\right], \; j = r, s,$$

and $\boldsymbol{z}$ is a unit length vector in $\{\boldsymbol{y}_0 - \boldsymbol{x}_s, \boldsymbol{y}_0 - \boldsymbol{x}_r\}^{\perp}$. With this choice, a direct calculation gives $\boldsymbol{U}_{j0}^*\boldsymbol{U}_{rs} = \mathrm{diag}(1, \cos(\theta_j))$, $j = r, s$. Therefore we get the SVD (up to a sign):

(89)
$$\boldsymbol{P}(\boldsymbol{x}_r, \boldsymbol{y}_0)\boldsymbol{P}(\boldsymbol{x}_s, \boldsymbol{x}_r)\boldsymbol{P}(\boldsymbol{y}_0, \boldsymbol{x}_s) = \boldsymbol{U}_{r0}\,\mathrm{diag}(1, \cos(\theta_r)\cos(\theta_s))\boldsymbol{U}_{s0}^*.$$

The rank and condition number identity follows. □

APPENDIX C. PROOF OF LEMMA 1

Proof. To prove (49), it is more convenient to use the rescaled array $\widetilde{\mathcal{A}} = a^{-1}\mathcal{A}$, where $\mathrm{mes}\,\widetilde{\mathcal{A}} = \mathcal{O}(1)$. We then follow the standard method based on integration by parts to study the asymptotic behavior of oscillating integrals (see e.g.[46]).

To this aim, we first rewrite the relation (41) as:
(90)
$$\widetilde{\boldsymbol{H}}_r(\boldsymbol{y}, \boldsymbol{y}'; k) = \frac{a^2 \exp[\imath k(\eta' - \eta)]}{(4\pi L)^2}\,\boldsymbol{P}_{\parallel}\int_{\widetilde{\mathcal{A}}} d\widetilde{\boldsymbol{x}}_{r,\parallel}\exp[\imath f(\widetilde{\boldsymbol{x}}_r)]$$

where f is defined on the rescaled array $\widetilde{\mathcal{A}}$ by
$$f(\widetilde{\boldsymbol{x}}_{r,\parallel}) = \frac{ka}{L}\left[\widetilde{\boldsymbol{x}}_r \cdot (\boldsymbol{y}_{\parallel} - \boldsymbol{y}'_{\parallel})\right] \text{ with } \widetilde{\boldsymbol{x}}_{r,\parallel} = \frac{\boldsymbol{x}_{r,\parallel}}{a} \in \widetilde{\mathcal{A}}.$$
Using the identity (which holds since $\nabla_{\widetilde{\boldsymbol{x}}_{r,\parallel}} f = (ka/L)(\boldsymbol{y}_{\parallel} - \boldsymbol{y}'_{\parallel})$ is constant):
$$\exp[\imath f] = \frac{1}{\imath}\,\mathrm{div}_{\widetilde{\boldsymbol{x}}_r}\left(\exp[\imath f]\,\frac{\nabla f_{\widetilde{\boldsymbol{x}}_r}}{|\nabla f_{\widetilde{\boldsymbol{x}}_r}|^2}\right),$$

and the divergence theorem applied to (90) yields

$$\widetilde{\boldsymbol{H}}_r(\boldsymbol{y}, \boldsymbol{y}'; k) = \frac{a^2 \exp[\imath k(\eta' - \eta)]}{(4\pi L)^2} \, \boldsymbol{P}_\parallel \, \frac{L}{ka|\boldsymbol{y}_\parallel - \boldsymbol{y}'_\parallel|} \, \int_{\partial\widetilde{\mathcal{A}}} \exp[\imath f] \, \frac{\nabla f_{\widetilde{\boldsymbol{x}}_r}}{\imath |\nabla f_{\widetilde{\boldsymbol{x}}_r}|} \cdot \boldsymbol{n},$$

where $\partial\widetilde{\mathcal{A}}$ is the boundary of $\widetilde{\mathcal{A}}$ and $\boldsymbol{n}$ is the outward pointing normal vector to $\partial\widetilde{\mathcal{A}}$. We conclude using the Cauchy-Schwarz inequality to get

$$\|\widetilde{\boldsymbol{H}}_r(\boldsymbol{y}, \boldsymbol{y}'; k)\| \le \frac{\operatorname{mes}\widetilde{\mathcal{A}} \, a^2}{(4\pi L)^2} \|\boldsymbol{P}_\parallel\| \, \frac{L}{ak|\boldsymbol{y}_\parallel - \boldsymbol{y}'_\parallel|} = \frac{a^2}{L^2} \, \mathcal{O}\Big(\frac{L}{a \, k|\boldsymbol{y}_\parallel - \boldsymbol{y}'_\parallel|}\Big).$$

Finally, the formula (50) follows from an immediate computation of the expression of (41) when $\boldsymbol{y}' = \boldsymbol{y}$. □

References

[1] H. Ammari, J. Chen, Z. Chen, J. Garnier, and D. Volkov, *Target detection and characterization from electromagnetic induction data*, Journal de mathématiques pures et appliquées, 101 (2014), pp. 54–75, `https://doi.org/10.1016/j.matpur.2013.05.002`.

[2] H. Ammari, J. Garnier, W. Jing, H. Kang, M. Lim, K. Sølna, and H. Wang, *Mathematical and statistical methods for multistatic imaging*, vol. 2098 of Lecture Notes in Mathematics, Springer, Cham, 2013, `https://doi.org/10.1007/978-3-319-02585-8`.

[3] H. Ammari, E. Iakovleva, D. Lesselier, and G. Perrusson, *MUSIC-type electromagnetic imaging of a collection of small three-dimensional inclusions*, SIAM J. Sci. Comput., 29 (2007), pp. 674–709, `https://doi.org/10.1137/050640655`.

[4] H. Ammari and A. Khelifi, *Electromagnetic scattering by small dielectric inhomogeneities*, Journal de mathématiques pures et appliquées, 82 (2003), pp. 749–842, `https://doi.org/10.1016/S0021-7824(03)00033-3`.

[5] H. Ammari, M. S. Vogelius, and D. Volkov, *Asymptotic formulas for perturbations in the electromagnetic fields due to the presence of inhomogeneities of small diameter II. The full Maxwell equations*, Journal de mathématiques pures et appliquées, 80 (2001), pp. 769–814, `https://doi.org/10.1016/S0021-7824(01)01217-X`.

[6] X. Antoine, B. Pinçon, K. Ramdani, and B. Thierry, *Far field modeling of electromagnetic time reversal and application to selective focusing on small scatterers*, SIAM J. Appl. Math., 69 (2008), pp. 830–844, `https://doi.org/10.1137/080715779`.

[7] R. Balan, P. Casazza, and D. Edidin, *On signal reconstruction without phase*, Appl. Comput. Harmon. Anal., 20 (2006), pp. 345–356, `https://doi.org/10.1016/j.acha.2005.07.001`.

[8] P. Bardsley and F. Guevara Vasquez, *Imaging with power controlled source pairs*, SIAM J. Imaging Sci., 9 (2016), pp. 185–211, `https://doi.org/10.1137/15M1023191`, `https://arxiv.org/abs/1507.00619`.

[9] P. Bardsley and F. Guevara Vasquez, *Kirchhoff migration without phases*, Inverse Problems, 32 (2016), p. 105006, `https://doi.org/10.1088/0266-5611/32/10/105006`, `https://arxiv.org/abs/1601.02667`.

[10] H. G. Berry, G. Gabrielse, and A. Livingston, *Measurement of the Stokes parameters of light*, Applied optics, 16 (1977), pp. 3200–3205.

[11] N. Bleistein, J. K. Cohen, and J. W. Stockwell, Jr., *Mathematics of multidimensional seismic imaging, migration, and inversion*, vol. 13 of Interdisciplinary Applied Mathematics, Springer-Verlag, New York, 2001, `https://doi.org/10.1007/978-1-4613-0001-4`. Geophysics and Planetary Sciences.

[12] L. Borcea and J. Garnier, *Robust imaging with electromagnetic waves in noisy environments*, Inverse Problems, 32 (2016), pp. 105010, 30, `https://doi.org/10.1088/0266-5611/32/10/105010`.

[13] L. Borcea, G. Papanicolaou, and F. Guevara Vasquez, *Edge illumination and imaging of extended reflectors*, SIAM Journal on Imaging Sciences, 1 (2008), pp. 75–114, `https://doi.org/10.1137/07069290X`.

[14] L. BORCEA, G. PAPANICOLAOU, AND C. TSOGKA, *Optimal waveform design for array imaging*, Inverse Problems, 23 (2007), pp. 1973–2020, `https://doi.org/10.1088/0266-5611/23/5/011`.

[15] M. BORN AND E. WOLF, *Principles of optics: Electromagnetic theory of propagation, interference and diffraction of light*, Pergamon Press, New York-London-Paris-Los Angeles, 1959.

[16] E. J. CANDÈS, T. STROHMER, AND V. VORONINSKI, *PhaseLift: exact and stable signal recovery from magnitude measurements via convex programming*, Comm. Pure Appl. Math., 66 (2013), pp. 1241–1274, `https://doi.org/10.1002/cpa.21432`.

[17] P. G. CASAZZA AND L. M. WOODLAND, *Phase retrieval by vectors and projections*, in Operator methods in wavelets, tilings, and frames, vol. 626 of Contemp. Math., Amer. Math. Soc., Providence, RI, 2014, pp. 1–17, `https://doi.org/10.1090/conm/626/12501`.

[18] M. CASSIER AND F. GUEVARA VASQUEZ, *Imaging polarizable dipoles*, SIAM J. Imaging Sci., 10 (2017), pp. 1381–1415, `https://doi.org/10.1137/17M112066X`.

[19] M. CASSIER AND C. HAZARD, *Multiple scattering of acoustic waves by small sound-soft obstacles in two dimensions: mathematical justification of the Foldy-Lax model*, Wave Motion, 50 (2013), pp. 18–28, `https://doi.org/10.1016/j.wavemoti.2012.06.001`.

[20] A. CHAI, M. MOSCOSO, AND G. PAPANICOLAOU, *Array imaging using intensity-only measurements*, Inverse Problems, 27 (2011), pp. 015005, 16, `https://doi.org/10.1088/0266-5611/27/1/015005`.

[21] Z. CHEN, S. FANG, AND G. HUANG, *A direct imaging method for the half-space inverse scattering problem with phaseless data*, Inverse Probl. Imaging, 11 (2017), pp. 901–916, `https://doi.org/10.3934/ipi.2017042`.

[22] Z. CHEN AND G. HUANG, *A direct imaging method for electromagnetic scattering data without phase information*, SIAM J. Imaging Sci., 9 (2016), pp. 1273–1297, `https://doi.org/10.1137/15M1053475`.

[23] Z. CHEN AND G. HUANG, *Phaseless imaging by reverse time migration: acoustic waves*, Numer. Math. Theory Methods Appl., 10 (2017), pp. 1–21, `https://doi.org/10.4208/nmtma.2017.m1617`.

[24] M. CHENEY, *The linear sampling method and the MUSIC algorithm*, Inverse Problems, 17 (2001), pp. 591–595, `https://doi.org/10.1088/0266-5611/17/4/301`. Special issue to celebrate Pierre Sabatier's 65th birthday (Montpellier, 2000).

[25] M. DE HOOP, S. HOLMAN, AND G. UHLMANN, *The method of stationary phase*, 2018 (accessed January 18, 2018), `http://maartendehoop.rice.edu/microlocal-analysis-inverse-problems/`.

[26] P. ELBAU, L. MINDRINOS, AND O. SCHERZER, *The inverse scattering problem for orthotropic media in polarization-sensitive optical coherence tomography*, GEM. Int. J. Geomath., online first (2017), pp. 1–21, `https://doi.org/10.1007/s13137-017-0102-y`.

[27] A. FREEMAN AND S. L. DURDEN, *A three-component scattering model for polarimetric SAR data*, IEEE Transactions on Geoscience and Remote Sensing, 36 (1998), pp. 963–973, `https://doi.org/10.1109/36.673687`.

[28] J. GARNIER AND G. PAPANICOLAOU, *Passive sensor imaging using cross correlations of noisy signals in a scattering medium*, SIAM J. Imaging Sci., 2 (2009), pp. 396–437, `https://doi.org/10.1137/080723454`.

[29] J. GARNIER AND G. PAPANICOLAOU, *Resolution analysis for imaging with noise*, Inverse Problems, 26 (2010), pp. 074001, 22, `https://doi.org/10.1088/0266-5611/26/7/074001`.

[30] J. GARNIER, G. PAPANICOLAOU, A. SEMIN, AND C. TSOGKA, *Signal-to-noise ratio estimation in passive correlation-based imaging*, SIAM J. Imaging Sci., 6 (2013), pp. 1092–1110, `https://doi.org/10.1137/120875533`.

[31] J. GARNIER, G. PAPANICOLAOU, A. SEMIN, AND C. TSOGKA, *Signal to Noise Ratio Analysis in Virtual Source Array Imaging*, SIAM J. Imaging Sci., 8 (2015), pp. 248–279, `https://doi.org/10.1137/140968677`.

[32] R. GERCHBERG AND W. SAXTON, *A practical algorithm for the determination of phase from image and diffraction plane pictures*, Optik, 35 (1972).

[33] N. R. GOODMAN, *Statistical analysis based on a certain multivariate complex Gaussian distribution. (An introduction)*, Ann. Math. Statist., 34 (1963), pp. 152–177, `https://doi.org/10.1214/aoms/1177704250`.

[34] A. Ishimaru, *Wave propagation and scattering in random media*, IEEE/OUP Series on Electromagnetic Wave Theory, IEEE Press, New York, 1997. Reprint of the 1978 original, With a foreword by Gary S. Brown, An IEEE/OUP Classic Reissue.

[35] M. V. Klibanov, *Uniqueness of two phaseless non-overdetermined inverse acoustics problems in 3-d*, Appl. Anal., 93 (2014), pp. 1135–1149, `https://doi.org/10.1080/00036811.2013.818136`.

[36] M. V. Klibanov and P. E. Sacks, *Phaseless inverse scattering and the phase problem in optics*, J. Math. Phys., 33 (1992), pp. 3813–3821, `https://doi.org/10.1063/1.529990`.

[37] M. V. Klibanov and P. E. Sacks, *Use of partial knowledge of the potential in the phase problem of inverse scattering*, J. Comput. Phys., 112 (1994), pp. 273–281, `https://doi.org/10.1006/jcph.1994.1099`.

[38] P. Mallet, C.-A. Guérin, and A. Santenac, *Maxwell-Garnett mixing rule in the presence of multiple scattering: Derivation and accuracy*, Phys. Rev. B, 72 (2009), p. 014205, `https://doi.org/10.1103/PhysRevB.72.014205`.

[39] L. Mandel and E. Wolf, *Optical coherence and quantum optics*, Cambridge University Press, 1995.

[40] M. Moscoso, A. Novikov, and G. Papanicolaou, *Coherent imaging without phases*, SIAM J. Imaging Sci., 9 (2016), pp. 1689–1707, `https://doi.org/10.1137/16M1064830`.

[41] M. Moscoso, A. Novikov, G. Papanicolaou, and C. Tsogka, *Multifrequency interferometric imaging with intensity-only measurements*, SIAM J. Imaging Sci., 10 (2017), pp. 1005–1032, `https://doi.org/10.1137/16M1105955`.

[42] A. Novikov, M. Moscoso, and G. Papanicolaou, *Illumination strategies for intensity-only imaging*, SIAM J. Imaging Sci., 8 (2015), pp. 1547–1573, `https://doi.org/10.1137/140994617`.

[43] L. Novotny and B. Hecht, *Principles of nano-optics*, Cambridge University Press, 2012.

[44] G. T. Schuster, *Seismic Interferometry*, Cambridge University Press, 2009.

[45] M. S. Vogelius and D. Volkov, *Asymptotic formulas for perturbations in the electromagnetic fields due to the presence of inhomogeneities of small diameter*, ESAIM: Mathematical Modelling and Numerical Analysis, 34 (2000), pp. 723–748, `https://doi.org/10.1051/m2an:2000101`.

[46] R. Wong, *Asymptotic approximations of integrals*, Computer Science and Scientific Computing, Academic Press, Inc., Boston, MA, 1989.

[47] P. Yin and J. Xin, *PhaseLiftOff: an accurate and stable phase retrieval method based on difference of trace and Frobenius norms*, Commun. Math. Sci., 13 (2015), pp. 1033–1049, `https://doi.org/10.4310/CMS.2015.v13.n4.a10`.